Fine-Tuning a Deconvolution Algorithm to Restore Displacement and Strain Maps Obtained with LSA

M. Grédiac, X. Balandraud, B. Blaysat, T. Jailin, R. Langlois, Frédéric Sur, A. Vinel

Fine-tuning a deconvolution algorithm to restore displacement and strain maps obtained with LSA

M. Grédiac[1*], X. Balandraud[1], B. Blaysat[1], T. Jailin[1], R. Langlois[1], F. Sur[2] and A. Vinel[1]

[1]Université Clermont Auvergne, Clermont Auvergne INP, CNRS, Institut Pascal, Clermont-Ferrand, F-63000, France.

[2]LORIA, UMR 7503, Université de Lorraine, CNRS, INRIA, Nancy, BP 239, 54506, France.

*Corresponding author(s). E-mail(s): michel.grediac@uca.fr;

Abstract

Background: Reliably measuring sharp details in displacement and strain maps returned by full-field measurement techniques remains an open question in the photomechanics community.

Objective: The primary objective of this study is to improve and fine-tune a deconvolution algorithm in order to limit the blur that obscures the details in displacement and strain maps.

Methods: Checkerboard patterns are used and processed with a spectral method, namely the Localized Spectrum Analysis (LSA), and the raw maps returned by this technique are deconvolved. The influence of various settings on the quality of the results is studied by using synthetic images deformed through a well-vetted reference displacement field.

Results: It is shown that linking the size of the analysis window used in LSA on the one hand, and the size of the second derivative kernel employed in the deconvolution algorithm on the other hand, ensures the convergence of the deconvolution algorithm in all cases. This was not the case with the initial version. The ratio between these sizes, which optimizes the metrological performance of LSA followed by deconvolution, is identified. The influence of the sampling density of the checkerboard

pattern in the images is also examined. The efficiency of the deconvolution algorithm employed with optimized settings is illustrated with strain maps obtained on two specimens, one in shape memory alloy, and the other in wood.

Conclusions: It is shown in this study that deconvolution with optimized settings is an effective tool to enhance small and sharp details in strain maps obtained with LSA.

Keywords: Deconvolution, Digital Image Correlation, Full-field measurement, Image restoration, Localized Spectrum Analysis, Metrology, Shape Memory Alloy, Wood

1 Introduction

Full-field measurement techniques are now widespread in the experimental mechanics community. Thanks to a good compromise between ease of use and metrological performance, Digital Image Correlation (DIC) is the most popular one. Assessing and improving the metrological performance of this measurement technique has garnered extensive research attention in this community, as illustrated by numerous papers recently published on this subject. This literature shows that DIC is well suited to situations for which the strain distribution gently spatially changes throughout the specimen. Capturing small details in those distributions is however much more challenging, if not impossible. The reason is that DIC behaves like a low-pass filter, so DIC cannot return small details which necessitate high-frequency spatial components to be correctly described if the corresponding frequencies are higher than the cutoff frequency of the corresponding filter. In addition, specific problems due to the fact that random speckles are used to mark the surface of the specimen arise, as recently pointed out in [1] with the Pattern-Induced Bias (PIB). Limiting if not removing PIB can be achieved by using periodic patterns like checkerboards instead of random ones. In addition, it has been shown that image gradient is maximized for such patterns [2], which leads sensor noise propagation to be minimized in the final displacement and strain maps. The problem is that classic versions of DIC cannot process periodic patterns. Even though it has been recently shown in [3] that a dedicated version of DIC could process such patterns, DIC basically relies on the iterative minimization of the optical residual, which makes this technique quite demanding in terms of computer resources. An alternative solution discussed in [4, 5] is to switch the minimization of the optical residual from the spatial to the frequency domain since this considerably speeds up the procedure without reducing the metrological performance. Specific spectral techniques such as the Localized Spectrum Analysis (LSA) can be used to reach this goal [6]. Like classic subset-based DIC [7, 8], a limitation is however that LSA does not directly return the true and sought

quantity, but this quantity convolved by a kernel, which is known a priori [9]. In general, the negative effect of convolution on displacement and strain maps cannot be directly removed by using classic deconvolution algorithms, the latter being developed under assumptions that are valid for natural images, not for displacement or strain maps [10]. In addition, the primary goal is not to render images that are pleasant to the eye but to provide measurement maps, which means that the errors must also be quantified. A deconvolution algorithm suitable for displacement or strain maps has been proposed in [11], but it is shown in this reference that this algorithm does not converge in all cases. In addition, the settings were not optimized.

In this context, the objective of this contribution is to improve the deconvolution algorithm introduced in [11] by *i*- ensuring convergence of this algorithm in any case, and *ii*- by proposing a setting such that the metrological performance of the deconvolution procedure is optimized. The paper is illustrated with simulations performed with synthetic images obtained with a suitable image rendering algorithm [12]. The optimized version of the deconvolution algorithm is finally applied in two real cases, for which it is of prime importance to render in a reliable way tiny details in strain maps.

The paper is organized as follows. First, we recall the basics of the different tools used in this study, namely the way synthetic checkerboard images are obtained and deformed through a well-vetted reference displacement field, the spectral method employed to process these images, and the deconvolution algorithm. The influence of various parameters governing the quality of the final results is examined in the second part, and optimized settings are deduced. The deconvolution algorithm with optimal setting is finally used in two real cases dealing with phase change in a shape memory alloy and the estimation of the strain field in a wood specimen embedding a knot. The definition of the four parameters characterizing the metrological performance discussed in the paper is given in a separate appendix.

2 Methods

2.1 A brief reminder on the Localized Spectrum Analysis

The gray level distribution of a checkerboard pattern can be regarded as the superposition of two signals denoted by frng, each being 2π-periodic along one of two perpendicular directions. These directions are the bisectors x_1''- and x_2'' of the natural axes of symmetry of the checkerboard, see Figure 1. This gives

$$s(x_1,x_2)=\frac{A}{2}\left(2+\gamma\mathsf{frng}\left(\frac{2\pi\sqrt{2}x_1''}{p}+\Phi_1''(x_1,x_2)\right)+\gamma\mathsf{frng}\left(\frac{2\pi\sqrt{2}x_2''}{p}+\Phi_2''(x_1,x_2)\right)\right) \tag{1}$$

where A is the average global field illumination, γ is the contrast. p is the nominal period of the periodic signals measured along its natural axes of symmetry

x'_1 or x'_2, so $\frac{\sqrt{2}}{2}p$ is the period along the bisectors x''_1 and x''_2 of the x'_1 and x'_2-directions. Φ''_1, Φ''_2 are the modulations of these two signals along the x''_1- and x''_2-directions, respectively. s, Φ''_1 and Φ''_2 are obtained over a grid of pixels, so they are given as a function of the coordinates of those pixels, namely x_1 and x_2.

Each displacement component measured along the x''_1- and x''_2-directions is proportional to the phase change along the corresponding direction. After a change of basis to get the displacement components in the x_1- and x_2-directions (denoted by u_1 and u_2, respectively), we have

$$u_i(x_1,x_2) = -\frac{1}{2\pi}\frac{\sqrt{2}}{2}p\left(\Phi_i^{cur}(x_1+u_1(x_1,x_2), y+u_2(x_1,x_2)) - \Phi_i^{ref}(x_1,x_2)\right) \quad i\in\{1,2\}. \tag{2}$$

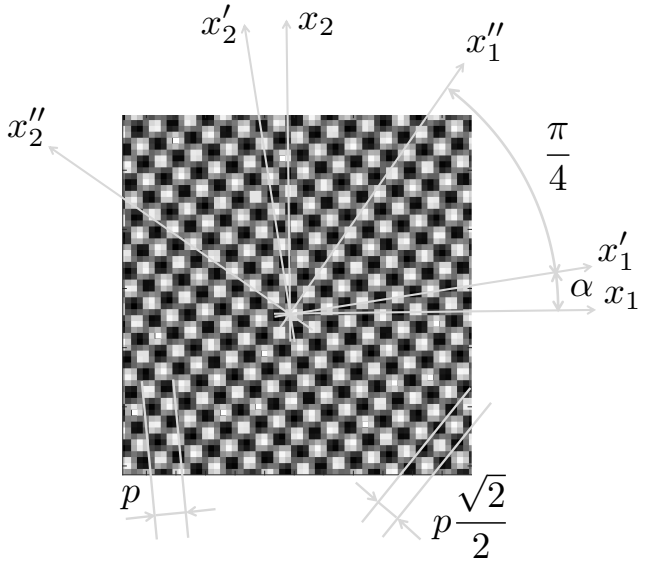

Fig. 1: Different coordinate systems involved in the calculation. Nominal period p of the checkerboard = twice the size of the squares forming the checkerboard. Period used to process the checkerboard images: $p\frac{\sqrt{2}}{2}$. (x_1, x_2) are the axes of the pixel coordinates, (x'_1, x'_2) are the so-called natural axes of symmetry of the checkerboard, and (x''_1, x''_2) define the directions rotated by +45 degrees with respect the x'_1 and x'_2 directions. They are called the bisectors in the following.

Determining $u_1(x_1, x_2)$ and $u_2(x_1, x_2)$ is not direct but quasi-direct, in the sense that the displacements along x_1 and x_2 appear in both parts of the equation. These quantities are found numerically by using a fixed-point

algorithm, which means that a first estimate is obtained by zeroing $u_1(x_1, x_2)$ and $u_2(x_1, x_2)$ in the right-hand side of Equation 2. This first estimate is then placed in the right-hand side of Equation 2, which enables us to determine a second and more precise estimate used in turn to feed the right-hand side of the equation, etc. The procedure quickly converges as the derivatives of the phases are such that

$$p/2\pi \|\nabla \Phi^{cur}\|_\infty < 1, \tag{3}$$

where $\|\cdot\|_\infty$ denotes the supremum of a function, as explained in [13]. In this case, the Banach fixed-point theorem [14] ensures the convergence of the algorithm. Since we are interested here in measuring small strains, which induce small phase derivatives, only one or two iterations at most are generally sufficient to reach convergence.

In Equation 2, Φ_i^{ref} and Φ_i^{cur}, $i \in \{1, 2\}$, are the phase distributions of this periodic pattern in the reference and current configurations, respectively. These two phases are deduced from the images by using a spectral technique. The Localized Spectrum Analysis (LSA) is one of these techniques [6]. With LSA, the first step is to calculate the windowed Fourier transform (WFT) of the signal (here the gray level distribution) s. The sought phase is then obtained by taking the argument of the resulting complex number distribution. This quantity is denoted by $\mathcal{F}_{w_{\mathsf{LSA}}}(s)$, where w denotes the analysis window. The WFT is calculated for only one spatial frequency f which is equal to the nominal frequency $f = \dfrac{\sqrt{2}}{p}$ of the periodic pattern, and for a direction defined by an angle θ with respect to the horizontal axis in Figure 1. This gives

$$\mathcal{F}_{w_{\mathsf{LSA}}}(s)(x_1, x_2, \theta) = \int_{-\infty}^{+\infty} \int_{-\infty}^{+\infty} s(\eta, \xi) w_{\mathsf{LSA}}(x_1 - \eta, x_2 - \xi) e^{-2i\pi f(\eta cos\theta + \xi sin\theta)} d\eta d\xi \tag{4}$$

with $i^2 = -1$. The analysis window w_{LSA} is centered at the pixel of coordinates x_1, x_2 where $\mathcal{F}_{w_{\mathsf{LSA}}}(s)(x_1, x_2, \theta)$ is calculated. The 2D Gaussian window defined by

$$w_{\mathsf{LSA}}(x_1, x_2) = \frac{1}{2\pi \ell_{\mathsf{LSA}}^2} e^{\left(-\dfrac{x_1^2 + x_2^2}{2\ell_{\mathsf{LSA}}^2}\right)} \tag{5}$$

constitutes the best tradeoff between various constraints, see [15] for 2D grids. This point is also discussed further in Section 5. In Equation 5, ℓ_{LSA} is the standard deviation of this Gaussian function. Similarly to the subset size in DIC, ℓ_{LSA} can be considered as a handy parameter which governs the apparent size of the analysis window used in LSA. However, contrary to the subset size in DIC, ℓ_{LSA} is a real-valued quantity.

The Gaussian function has no compact support. Its apparent width is classically arbitrarily considered to be equal to $6 \times \ell_{\mathsf{LSA}}$ according to the so-called "$3 - \sigma$ rule" [16]. Figure 2 (a) shows the Gaussian analysis window plotted

with $\ell_{\mathsf{LSA}} = 9.3$ [px]. Its apparent size is equal to $6 \times 9.3 \simeq 56$ [px] according to this rule. In practice, the size of the support used in the calculation is finite and must be greater than this apparent size. In the calculations performed in this paper, the size of this support was equal to $2 \times \mathsf{ceil}(4 \times \ell_{LSA}) + 1$, where $\mathsf{ceil}(.)$ denotes the smallest integer number larger than ".". In the present case, this gives $2 \times 38 + 1 = 77$ [px]. Note that the Gaussian analysis window strictly integrates to one over this compact support. This property is simply obtained by dividing the expression given in Equation 5 by its integral calculated over this support.

In Equation 4, θ represents the angle of the direction along which the WFT is calculated. This WFT is calculated along two directions since 2D displacement components must be calculated. These two directions are $\theta = \alpha + \frac{\pi}{4}$ and $\theta = \alpha + \frac{3\pi}{4}$, where α is the angle which gives the orientation of the natural axes of symmetry of the periodic pattern with respect to the (x_1, x_2) axes, see Figure 1. $\alpha \neq 0$ in order to avoid aliasing in the images, see [17].

Compared to other spectral techniques, a big advantage of LSA is the short computing time. The main reason is the fact that a Fast Fourier Transform is employed to switch the calculation from the spatial to the frequency domain. Another reason is the fact that the argument of $\mathcal{F}(w_{\mathsf{LSA}})(x_1, x_2, \theta)$ is generally considered to be directly equal to the phase of the periodic signal involved in Equation 2. However and as demonstrated in [9], the argument of $\mathcal{F}_{w_{\mathsf{LSA}}}(s)(x_1, x_2, \theta)$ is well approximated by the convolution of the true (and sought) phase along θ and the analysis window w_{LSA}. The idea is thus to deconvolve the phase maps obtained with LSA to retrieve the true phase distributions, or at least a quantity closer to the true phase distributions than their convolved versions, and eventually a better estimation of the displacement field.

2.2 Synthetic displacement field

Pairs of synthetic checkerboard images in reference and in deformed configurations were used here to assess this metrological performance. They were obtained with a program named CheckerboardRender available online [1]. This program works with the same principle as BSpekleRender introduced in [12] to render random speckles suitable for DIC. Its major benefit is to render synthetic images which are not affected by interpolation. The checkerboard pattern was rotated by $\alpha = 10$ degrees. Eight different sampling densities ρ were used to generate the checkerboard images in order to examine the influence of this parameter on the results. ρ was equal to 5.3 to 12.3 pixels/period, with a step equal to 1.0 pixels/period. These non-integer values more faithfully reproduce what happens in real experiments because having integer values for ρ requires a precise but tedious setting of the optical device and of the respective positions of the specimen and the camera. Noiseless and noisy images were obtained in each case, with a variance of the noise σ_{image} modelled by

[1] https://members.loria.fr/FSur/software/BSpeckleRender/

an affine function of the gray level, as suggested in [18]. The slope a is equal to $a = 0.0342$, and the intercept to $b = 0.2679$. These are typical values for a digital camera. The dimensions of the synthetic checkerboard images were 501×2000 [px^2] along the vertical and horizontal axes, respectively, They were slightly deformed with a sine wave along the x_2-direction of period p_{wave}, this period lying between 10 and 150 pixels, the displacement $u_1(x_1, x_2)$ along the x_1-direction being null. The amplitude of the wave is equal to 0.5 [px], this quantity corresponding to a case for which the interpolation bias is null when the images are processed with DIC. This is not the case here but we stick with this value to be consistent with other studies where such a reference displacement field is used, and the images processed with DIC, see [5, 19] for instance. The reference displacement field along the x_2 direction is such that the period gently increases from the left to the right. The closed-form expression of the u_2 displacement reads as follows:

$$u_2(x_1, x_2) = 0.5 \times \cos\left(\frac{2\pi}{p_{wave}}\left(x_2 - \frac{H+1}{2}\right)\right) \tag{6}$$

with

$$p_{wave} = p_{wave}^{mini} + \frac{p_{wave}^{maxi} - p_{wave}^{mini}}{L-1}(x_1 - 1) \tag{7}$$

H and L are the height and the length of the map, respectively. p_{wave}^{mini} and p_{wave}^{mini} are the minimum and maximum values of the period of the wave respectively. In the present case, we have $L = 2000$ [px], $H = 501$ [px], p_{wave}^{mini} =10 [px] and $p_{wave}^{maxi} = 150$ [px]. The u_2 displacement field is represented in Figure 3. This displacement field is suitable for the analysis of the progressive damping of the amplitude of the sine wave returned by the measuring system when the frequency of this wave increases, thus when going to the left-hand side of the map. The curve representing the cross-section of this field along the horizontal midline (denoted by Δ in Figure 3) is generally plotted to study in depth this damping. This type of synthetic displacement has already been used in previous papers dealing with the metrological performance of full-field measurement methods, see [4, 5, 10, 19–22]. It was christened the "STAR" displacement field in [19].

2.3 Deconvolving phase maps to reduce the bias

A deconvolution algorithm dedicated to phase maps obtained by LSA has been proposed in Ref. [23]. Deconvolving phase maps leads to an enhancement of the quality of these maps, as well as that of the displacement and strain fields returned by the measuring technique. More precisely, the spatial resolution (the definition of this quantity is given in the Appendix) becomes smaller (thus better), which enables us to sharpen details in strain maps. The noise level increases but in a lower proportion. This leads the sum of the random error and the systematic error to be lower after deconvolution, the decrease of this total

error being significant for "intermediate" spatial frequencies, as illustrated in the results of the numerical simulations discussed in the following sections.

Deconvolution procedures are generally performed under appropriate assumptions concerning the problem at hand, in order to make the procedure robust to noise. Compared to natural images of everyday life (and even images of patterns used in photomechanics like random speckles or checkerboards), phase or displacement maps much more gently spatially change, apart from in the case of cracks where they become discontinuous. The deconvolution procedure proposed in [23] thus consists in considering the Taylor expansion of the convolution product between the true (and sought) phases gathered in vector $\underline{\Phi}^{true}$, and the analysis window w_{LSA} used in LSA. This leads to the following link between $\underline{\Phi}^{true}$ and the vector $\underline{\Phi}$ containing the phases returned by LSA:

$$\underline{\Phi}^{true} = \underline{\Phi} - \delta\underline{\Phi} \tag{8}$$

After mild approximations (see details in Ref. [23]), the equation above gives the following iterative procedure to estimate the correction of the phases returned by LSA:

$$\begin{cases} \underline{\widetilde{\Phi}}^{0} = \underline{\Phi} \\ \underline{\widetilde{\Phi}}^{\mathsf{it}+1} = \underline{\Phi} - \delta\underline{\widetilde{\Phi}}^{\mathsf{it}}, \text{ with } \delta\underline{\widetilde{\Phi}}^{\mathsf{it}} = \dfrac{1}{2} \displaystyle\sum_{i=\{u,v\}} \sum_{k,l=1}^{2} \widetilde{\Phi}^{\mathsf{it}}_{i,kl}\, I_{kl}\, \underline{e}_i \end{cases}, \tag{9}$$

The procedure returns a vector $\underline{\widetilde{\Phi}}$, whose components are closer to the components of $\underline{\Phi}^{true}$ than the components of $\underline{\Phi}$. In this equation, $\widetilde{\Phi}^{\mathsf{it}}_{i,kl}$ is the second derivative of $\widetilde{\Phi}^{\mathsf{it}}$ with respect to directions k and l at the it-th iteration. u and v are the directions along which $\underline{\widetilde{\Phi}}$ is determined, x_1 and x_2 since in practice, deconvolution is applied to the phases expressed in the x_1 and x_2 directions. I_{kl} is the second moment of the kernel w_{Hess} with respect to the x_k and x_l directions, $k, l \in \{1, 2\}$. It is defined as follows:

$$I_{kl} = \iint_{(\eta_1,\eta_2)\in\Re^2} w_{\mathsf{Hess}}(\eta_1, \eta_2)\eta_k\eta_l \, \mathrm{d}\eta_1 \, \mathrm{d}\eta_2 \tag{10}$$

In Equation 9, the second derivatives are estimated by convolving the two components of $\underline{\widetilde{\Phi}}^{\mathsf{it}}$ with a second-order derivative kernel, chosen here as a classic "Mexican hat" aligned with the direction(s) of derivation. Such a kernel is defined by the second derivatives of a Gaussian distribution defined by a standard deviation denoted by ℓ_{Hess}. For instance, the second derivative of a phase map along x_1 is obtained by convolving this phase map by the second derivative of the following Gaussian function with respect to x_1:

$$w_{\mathsf{Hess}}(x_1, x_2) = \frac{1}{2\pi\ell^2_{\mathsf{Hess}}} e^{\left(-\dfrac{x_1^2 + x_2^2}{2\ell^2_{\mathsf{Hess}}}\right)}, \tag{11}$$

which gives

$$\frac{\partial w^2_{\mathsf{Hess}}(x_1,x_2)}{\partial x_1^2} = -\frac{1}{2\pi\ell^4_{\mathsf{Hess}}}\left(1-\frac{x_1^2}{\ell^2_{\mathsf{Hess}}}\right)e^{\left(-\frac{x_1^2+x_2^2}{2\ell^2_{\mathsf{Hess}}}\right)}. \tag{12}$$

With the numerical implementation of this kernel, it is important to check that

$$\iint_{(\eta_1,\eta_2)\in\mathsf{D}} \frac{\partial w^2_{\mathsf{Hess}}(\eta_1,\eta_2)}{\partial x^2}\,\mathrm{d}\eta_1\,\mathrm{d}\eta_2 = 0 \tag{13}$$

where D is the domain over which the second derivative kernel is estimated. Since the support is compact and not infinite, this integral is nullified by adding a suitable constant to this second derivative. The same remark holds for the other components of the Hessian.

The opposite of the second derivative filter along x_1 (denoted by $w_{\mathsf{Hess},11}$) is depicted in Figure 2 (b) with $\frac{\ell_{\mathsf{Hess}}}{\ell_{\mathsf{LSA}}} = 0.67$ [-] and $\ell_{\mathsf{LSA}} = 9.3$ [px], as for the Gaussian analysis window shown in Figure 2 (a). 0.67 is a particular value that will be justified later in the paper. It can be seen that the apparent size of this kernel is visually smaller than the apparent size of the Gaussian analysis window. The support of this kernel used in the calculations must be greater than the apparent size visually observed in Figure 2 (b). In the present paper, the size of this support was equal to $2\times\mathsf{ceil}(6\times\ell_{Hess})+1$. With this example, this again gives $2\times 38+1 = 77$ [px], as for the Gaussian analysis window, but the size of this support is in general different from the size of the support of the Gaussian analysis window.

The main steps of the deconvolution procedure are given in Algorithm 1.

Algorithm 1 Deconvolution of a phase map

1: **input**: $\underline{\Phi}$: phase map to be restored, w_{Hess}: second-order derivative kernel
2: $I_{kl} \leftarrow \iint_{(\eta_1,\eta_2)\in\Re^2} w_{\mathsf{Hess}}(\eta_1,\eta_2)\eta_k\eta_l\,\mathrm{d}\eta_1\,\mathrm{d}\eta_2$ for any $k,l\in\{1,2\}$
3: **initialisation**: it $= 0$, $\underline{\Phi}^0 = \underline{\Phi}$
4: **while** it ≤ 10 **do**
5: $\quad\delta\widetilde{\underline{\Phi}}^{\mathsf{it}} \leftarrow \frac{1}{2}\sum_{i=\{u,v\}}\sum_{k,l=1}^{2}\widetilde{\Phi}^{\mathsf{it}}_{i,kl}\,I_{kl}\,\underline{e}_i$
6: $\quad\widetilde{\underline{\Phi}}^{\mathsf{it}+1} \leftarrow \widetilde{\underline{\Phi}} - \delta\widetilde{\underline{\Phi}}^{\mathsf{it}}$
7: $\quad$it $\leftarrow$ it $+ 1$
8: **end while**
9: **output:** deconvolved phase map

A key point in this procedure is the choice of the size of the support over which the second-derivative filter is defined. This size is governed by ℓ_{Hess}. In Ref.[23], ℓ_{Hess} was constant whatever the value of ℓ_{LSA}, and it was observed that the procedure converged only for values of ℓ_{LSA} lower than or close to the nominal period p of the checkerboard. This procedure diverged for greater values, which was a limitation. We will see below that choosing ℓ_{Hess} to be

proportional to ℓ_{LSA} and suitably adjusting the proportion between these two quantities leads the deconvolution procedure to converge for all the values tested in this study, which covers a range including usual values of the size of the analysis window, thus of ℓ_{LSA}.

2.4 Impact of convolution/deconvolution on the displacement and strain maps

Displacement maps are deduced from the phase maps by using Equation 2 and the associated fixed-point algorithm. This algorithm does not equally affect all the pixels of the phase distributions when the displacement is retrieved. Consequently and strictly speaking, displacement maps obtained by LSA and the fixed-point algorithm are not directly the true displacement maps convolved by the analysis window. However, this spatial fluctuation may reasonably be considered as sufficiently small to be neglected compared to the effect of convolution. Thus, displacement maps deduced from Equation 2 will be considered as convolved by the analysis window even though they are deduced from the convolved phases with Equation 2 and the associated fixed-point algorithm. In the same way, if deconvolved phase maps are used in this equation, the resulting displacement field will also be considered as the deconvolved one.

Concerning strain, it is worth remembering that the derivative of the convolution of two functions is the convolution of one of the functions with the derivative of the other. Thus, the following equations holds for any functions g and w:

$$(g \otimes w)' = g \otimes w' = g' \otimes w \tag{14}$$

where symbol $'$ denotes derivation and $\otimes$ convolution. Considering here that g is one of the two displacement components u_1 or u_2, and w the analysis window w_{LSA} used in LSA, it means that the convolution by the analysis window affects in the same way both the displacement and the strain maps.

We now consider the particular case of the reference displacement field presented in Section 2.2 and the corresponding ε_{22} component. The closed-form expression of the ε_{22} strain distribution can be deduced from the expression of u_2 given in Equation 6. This leads to:

$$\varepsilon_{22} = -0.5 \times \frac{2\pi}{p_{wave}} \times \sin\left(\frac{2\pi}{p_{wave}}\left(x_2 - \frac{H+1}{2}\right)\right) \tag{15}$$

In the particular case considered here, the relative change in amplitude of both the u_2 displacement and the ε_{22} strain components are the same. It means that if the real displacement field is dominated by a given cosine distribution along a direction, the strain field along this direction is dominated by a sine wave featuring the same period. Consequently, the relative change in amplitude is the same for both the displacement and the strain along this direction. This remark will turn out to be useful in Section 8.1, where a real strain map will be discussed. Note that this remark is not valid in the general case, the local

response being influenced by numerous harmonics, with coefficients being not proportional between displacement and strain distributions.

2.5 Influencing parameters

In conclusion, considering that the analysis window w_{LSA} used in the LSA procedure is a 2D Gaussian function, the quality of the results obtained with LSA and deconvolution is mainly governed by three parameters:

- The width of this Gaussian analysis window, which is proportional to its standard deviation ℓ_{LSA}.
- The width of the second-derivative filter used to estimate the Hessian of the phase distributions. This filter is a "Mexican hat" deduced by double derivation from a 2D Gaussian function denoted by w_{Hess}. Its standard deviation, denoted by ℓ_{Hess}, also governs the size of this window.
- The sampling density ρ [px/period], which is equal to the number of pixels per nominal period p of the checkerboard. The minimum value for ρ enabling to correctly encode the squares of a checkerboard is equal to 5 pixels [11], but the usual values for this quantity in real experiments is close to 6 to limit the negative effect of the Point Spread Function of the lens, as underlined in [24]. This value is consistent with the average number of 3 pixels per dot recommended in [25] for correctly sampling dots in random speckles used with DIC.

To make the results comparable between different values of ρ, the first two parameters ℓ_{LSA} and w_{Hess} are normalized with respect to this quantity, as well as the period p_{wave} defined in Equation 7, the cutoff frequency $f_{c(\lambda)}$ and the Metrological Efficiency Indicator MEI defined in the Appendix. This gives:

$$\widetilde{\ell}_{\mathsf{LSA}} = \frac{\ell_{\mathsf{LSA}}}{\rho}, \quad \widetilde{\ell}_{\mathsf{Hess}} = \frac{\ell_{\mathsf{Hess}}}{\rho}, \quad \widetilde{p}_{wave} = \frac{p_{wave}}{\rho}, \quad \widetilde{f}_{c(\lambda)} = f_{c(\lambda)}\rho, \quad \widetilde{\mathrm{MEI}} = \frac{\mathrm{MEI}}{\rho}, \tag{16}$$

These normalized parameters will be used in the following. Changing the sampling density to encode the periodic signal can be interpreted, *ceteris paribus*, as a change in the distance between camera and specimen. This is not strictly the case in the synthetic images considered in the simulations since the amplitude of the reference displacement field defined in Section 2.2 is equal to 0.5 [px] whatever the value of ρ, which means that the real amplitude (in [m]) of the sine wave in those images changes from a value of ρ to another. The consequence is that the displacement resolution σ_u (see definition in the Appendix) was not normalized here. Indeed, since the amplitude of the sine wave remains the same (0.5 [px]) as the value of ρ changes, σ_u is already a parameter, which is normalized with respect to ρ.

Note finally that the deconvolution procedure described in Algorithm 1 is iterative, so the number of iterations is also a potential influencing parameter. However, it has been observed that the solution is only marginally refined

when using more than 10 iterations. All the results discussed in this paper were therefore obtained with a number of iterations equal to 10.

In the following, we will investigate the influence of the value of these three user-defined parameters, namely $\widetilde{\ell}_{LSA}$, $\widetilde{\ell}_{Hess}$ and ρ, on the quality of the results obtained after deconvolution, the objective being to get optimized values when it is possible, or to have a clear view on the influence of these parameters on the quality of the results.

3 Benefit of choosing $\widetilde{\ell}_{\mathsf{Hess}}$ proportional to $\widetilde{\ell}_{\mathsf{LSA}}$ on the convergence of the deconvolution algorithm

We illustrate here the benefit of adjusting the size of the second-derivative kernel used to calculated the Hessian, to the size of the analysis window used to extract the phase distributions field from the checkerboard images, thus $\widetilde{\ell}_{\mathsf{Hess}}$ to $\widetilde{\ell}_{\mathsf{LSA}}$. In Ref. [23], the size of the former was considered as a constant but the deconvolution procedure progressively diverged as $\widetilde{\ell}_{\mathsf{LSA}}$ became greater than one, which is a strong limitation. We show here that choosing a value of $\widetilde{\ell}_{\mathsf{Hess}}$ proportional to $\widetilde{\ell}_{\mathsf{LSA}}$ and correctly setting this proportion ensures the deconvolution algorithm to converge in all the cases that were tested. The intuitive explanation of this trick is that the variations of the convolved phase have a scale proportional to the size of the convolution kernel, thus to $\widetilde{\ell}_{\mathsf{LSA}}$. Consequently, it makes sense to measure these variations with a derivative kernel with a standard deviation $\widetilde{\ell}_{\mathsf{Hess}}$ proportional to $\widetilde{\ell}_{\mathsf{LSA}}$.

Figure 4 is a typical example of the improvement caused by having $\widetilde{\ell}_{\mathsf{Hess}}$ proportional to $\widetilde{\ell}_{\mathsf{LSA}}$ instead of having $\widetilde{\ell}_{\mathsf{Hess}}$ equal to a constant value. In this example, the sampling density ρ is equal to 6.3 pixels/period (results obtained with other values of ρ are discussed in Section 6). The calculations were performed with different values of $\widetilde{\ell}_{\mathsf{LSA}}$ lying between $\frac{\sqrt{2}}{2}$ and $3.0 \times \frac{\sqrt{2}}{2}$ [-], with a step of $0.1 \times \frac{\sqrt{2}}{2}$] [-]. Thus $\widetilde{\ell}_{\mathsf{LSA}} \in \{1.0 \times \frac{\sqrt{2}}{2}, 1.1 \times \frac{\sqrt{2}}{2}, \cdots, 2.9 \times \frac{\sqrt{2}}{2}, 3.0 \times \frac{\sqrt{2}}{2}\}$ [-].

We consider first the case for which the value of $\widetilde{\ell}_{\mathsf{Hess}}$ remains constant for all values of ℓ_{LSA}. This constant value is the same as that used in Ref. [23], where we had $\ell_{\mathsf{Hess}} = 2.1 \times 2 = 4.2$ pixels and $\rho = 6$[px/period], thus $\widetilde{\ell}_{\mathsf{Hess}} = 4.2/6 = 0.70$ for any value of ℓ_{LSA}. Figure 4 (a) shows the u_2 displacement along the midline Δ found in this case. The curves obtained after deconvolution show that the algorithm converges for the smallest values of $\widetilde{\ell}_{\mathsf{LSA}}$. The curve exhibits large fluctuations when $\widetilde{\ell}_{\mathsf{LSA}}$ becomes greater than about $1.4 \times \frac{\sqrt{2}}{2} \simeq 1$ [-]. Indeed, the difference between the curves corresponding to the successive steps of the iterative procedure monotonically increases. Since this phenomenon becomes more pronounced as $\widetilde{\ell}_{\mathsf{LSA}}$ increases, the curves corresponding to $\widetilde{\ell}_{\mathsf{LSA}} > 1.8 \times \frac{\sqrt{2}}{2}$ [-] are not shown in this figure.

In Figure 4 (b), the value of $\widetilde{\ell}_{\mathsf{Hess}}$ is no longer constant, but proportional to the value of $\widetilde{\ell}_{\mathsf{LSA}}$, with $\widetilde{\ell}_{\mathsf{Hess}} = 0.70 \times \widetilde{\ell}_{\mathsf{LSA}}$. This value of 0.70 is obtained by

dividing the constant value of $\widetilde{\ell}_{\mathsf{Hess}}$ used in [23] (4.2 [px]) by the nominal period of the checkerboard used in this reference, namely $p = 6$ [px]. Figure 4 (b) shows that the algorithm converges whatever the 21 values of $\widetilde{\ell}_{\mathsf{LSA}}$ tested in this study, which illustrates the fact that $\widetilde{\ell}_{\mathsf{Hess}}$ should be proportional to $\widetilde{\ell}_{\mathsf{LSA}}$.

This phenomenon can be regarded as a scale effect. Indeed, since LSA returns the true phase convolved by the analysis window used in LSA, increasing the size of this analysis window causes a wider zone to be affected by this convolution. It seems therefore logical to adjust in proportion the size of the zone over which the Hessian is estimated. In Figure 4 (b), it is worth noting that the curves obtained after deconvolution are regularly spaced. They are shifted to the right as $\widetilde{\ell}_{\mathsf{LSA}}$ stepwise increases, which means that the spatial resolution $\frac{1}{f_{c(-10\%)}}$ as defined in the Appendix regularly decreases. We will see in Section 7 that this shift is rigorously proportional to $\widetilde{\ell}_{\mathsf{LSA}}$.

The preceding figures were obtained with noiseless synthetic images. Non-blind deconvolution (in the sense that the kernel is known *a priori*, blind deconvolution meaning that this kernel is unknown) is however an ill-posed problem in the presence of noise, so it is important to check the robustness of the algorithm in this case. Figure 4 (c) shows the same types of curves as those shown in Figure 4 (b), but this time with displacement maps retrieved from pairs of noisy images. Noise is characterized by the values of a and b given in Section 2.2. The curves are therefore noisy, and the noise is all the higher as the analysis window used in LSA decreases (from the light blue to the dark blue curves). However, the important point is that deconvolution still converges with noisy data. In addition, the amplitude of the noise after deconvolution remains reasonable, which illustrates the robustness of the procedure. It is observed that lower noise levels are obtained with greater values of the $\frac{\widetilde{\ell}_{\mathsf{Hess}}}{\widetilde{\ell}_{\mathsf{LSA}}}$ ratio, as discussed in the following section. This is a consequence of the fact that a greater number of pixels is involved in the calculations when this ratio increases, which leads to more efficiently smoothing out this noise.

4 Optimizing the ratio between $\widetilde{\ell}_{\mathsf{Hess}}$ and $\widetilde{\ell}_{\mathsf{LSA}}$

The ratio between $\widetilde{\ell}_{\mathsf{Hess}}$ and $\widetilde{\ell}_{\mathsf{LSA}}$ is now investigated in detail in order to see if an optimal value can be found.

As a general remark, increasing the value of $\widetilde{\ell}_{\mathsf{Hess}}$ for a given and fixed value of $\widetilde{\ell}_{\mathsf{LSA}}$ increases the zone over which the Hessian is calculated. This should therefore increase the blur and decrease (thus deteriorate) the cutoff frequency beyond which high-frequency details cannot be retrieved. The counterpart is to decrease (thus improve) the displacement resolution because the number of pixels covered by the second-derivative kernel increases, thus averaging the effect of noise over a wider zone. At the same time and for the same reason as for $\widetilde{\ell}_{\mathsf{Hess}}$, the value of $\widetilde{\ell}_{\mathsf{LSA}}$ directly influences both the spatial resolution and the measurement resolution. As a conclusion, two parameters influence the two latter metrological parameters of the measuring technique: namely $\widetilde{\ell}_{\mathsf{Hess}}$ and $\widetilde{\ell}_{\mathsf{LSA}}$, and the goal here is to estimate the best ratio between the two since

they should be proportional to ensure the convergence of the deconvolution algorithm.

In this section, we first show that for a given value of $\widetilde{\ell}_{\mathsf{LSA}}$, two regimes can be distinguished when examining the influence of $\widetilde{\ell}_{\mathsf{Hess}}$. Second, both the values of $\widetilde{\ell}_{\mathsf{LSA}}$ and $\widetilde{\ell}_{\mathsf{Hess}}$ are changed in order to span a space of reasonable values for these quantities, and see if an optimal solution emerges for the ratio between the two.

4.1 Existence of two regimes

As an example, we consider first that the value of $\widetilde{\ell}_{\mathsf{LSA}}$ is fixed, with $\widetilde{\ell}_{\mathsf{LSA}} = \dfrac{\sqrt{2}}{2}$ [-] (in Figure 4 (b), this corresponds to the fifth curve obtained from the lowest possible value of $\widetilde{\ell}_{\mathsf{LSA}}$). The corresponding value of $\widetilde{\ell}_{\mathsf{LSA}}$ is the closest to 1.00 since $1.40 \times \frac{\sqrt{2}}{2} \simeq 1$. Thus ℓ_{LSA} is close to the nominal period of the checkerboard expressed in pixels. $\widetilde{\ell}_{\mathsf{LSA}}$ being fixed, $\widetilde{\ell}_{\mathsf{Hess}}$ stepwise increases from 0.60 to 1.0 [-], with a step equal to 0.02 [-]. Other values of $\widetilde{\ell}_{\mathsf{LSA}}$ will be discussed in the following section. The value of the sampling density is fixed here to 6.3 pixels/period.

Figure 5 (a) shows various curves which are cross-sections along Δ of the displacement field retrieved with noiseless images and after deconvolution, with $\widetilde{\ell}_{\mathsf{LSA}} = \frac{\sqrt{2}}{2} \times 1.4$ [-], and $\widetilde{\ell}_{\mathsf{Hess}}$ stepwise increasing from $1.0 \times \frac{\sqrt{2}}{2}$ to $3.0 \times \frac{\sqrt{2}}{2}$ with a step equal to $0.1 \times \frac{\sqrt{2}}{2}$. When $\widetilde{\ell}_{\mathsf{Hess}}$ decreases, the color of the curves turns from light to dark blue. It can be observed that decreasing the value of $\widetilde{\ell}_{\mathsf{Hess}}$ progressively straightens out the curves, which causes the spatial resolution $\frac{1}{\widetilde{f}_{c(-10\%)}}$ to decrease. Two regimes can be distinguished. Indeed, for the lowest values of $\widetilde{\ell}_{\mathsf{Hess}}$ (curves plotted in dark blue), the curves remain above the reference amplitude of 0.5 pixel on the left-hand side of the figure, see "Regime A" reported in Figure 5 (a). For the highest values of $\widetilde{\ell}_{\mathsf{Hess}}$ (curves plotted in light blue), the curves are strictly monotonic and remain under the red horizontal line representing the reference value of 0.5 pixel, see "Regime B". Additional simulations performed with a smaller value of the increase between consecutive values of $\widetilde{\ell}_{\mathsf{Hess}}$ show that the limit between these two regimes is obtained with about $\frac{\widetilde{\ell}_{\mathsf{Hess}}}{\widetilde{\ell}_{\mathsf{LSA}}} = 0.72$, see the green curve plotted in Figure 5 (a).

Finding the value of $\widetilde{\ell}_{\mathsf{Hess}}$ for which $\lambda = +10\%$ is reached can be done by adjusting the value of $\widetilde{\ell}_{\mathsf{Hess}}$ in such a way that the curve after deconvolution is tangent to the red horizontal dashed line with dots corresponding to $\lambda = +10\%$. This numerical value is chosen to be consistent with previous studies dealing with the metrological performance of full-field measurement systems, in which a loss of amplitude of 10% was chosen to determine the cutoff frequency and the spatial resolution, [5, 19] for instance.

On close inspection of the different curves plotted in Figure 5 (a), it can be seen that the value of the $\frac{\widetilde{\ell}_{\mathsf{Hess}}}{\widetilde{\ell}_{\mathsf{LSA}}}$ ratio should lie between $\frac{\widetilde{\ell}_{\mathsf{Hess}}}{\widetilde{\ell}_{\mathsf{LSA}}} = 0.64$ and

$\frac{\widetilde{\ell}_{\mathsf{Hess}}}{\widetilde{\ell}_{\mathsf{LSA}}} = 0.66$. Refining further this search leads to a value of $\frac{\widetilde{\ell}_{\mathsf{Hess}}}{\widetilde{\ell}_{\mathsf{LSA}}}$ equal to 0.6515. This parameter corresponds to the lowest possible value of the $\frac{\widetilde{\ell}_{\mathsf{Hess}}}{\widetilde{\ell}_{\mathsf{LSA}}}$ ratio for which the maximum value of λ is equal to +10%. For higher values of $\widetilde{\ell}_{\mathsf{Hess}}$, the peak observed in the different curves of Regime A progressively vanishes, then switching from Regime A to Regime B for $\frac{\widetilde{\ell}_{\mathsf{Hess}}}{\widetilde{\ell}_{\mathsf{LSA}}} = 0.72$.

Considering that the value of λ should remain lower than +10 %, the lowest possible value of the spatial resolution $\frac{1}{\widetilde{f}_{c(-10\%)}}$ is obtained by considering Regime A and the steepest and leftmost curve that can be plotted while keeping an absolute value of λ lower than +10%, see the blue curve in Figure 5 (b). Point M gives the spatial resolution beyond which the amplitude is returned with a value of λ bounded by ±10%. It is obtained with the lowest possible value of the $\frac{\widetilde{\ell}_{\mathsf{Hess}}}{\widetilde{\ell}_{\mathsf{LSA}}}$ ratio. Decreasing this ratio causes the maximum value of λ to be greater than +10%.

These two regimes were described here for a particular value of $\widetilde{\ell}_{\mathsf{LSA}}$, but they can be observed for any value of $\widetilde{\ell}_{\mathsf{LSA}}$.

4.2 Seeking the optimal $\frac{\widetilde{\ell}_{\mathsf{Hess}}}{\widetilde{\ell}_{\mathsf{LSA}}}$ ratio

The objective here is to find the optimal $\frac{\widetilde{\ell}_{\mathsf{Hess}}}{\widetilde{\ell}_{\mathsf{LSA}}}$ ratio. This is the ratio, which leads to the lowest value of $\widetilde{\mathrm{MEI}}$. This is justified by the fact that the settings should ideally lead to the highest possible cutoff frequency for a given value of λ, but ever smaller values of $\widetilde{\ell}_{\mathsf{Hess}}$ must be considered to reach this goal for a given value of $\widetilde{\ell}_{\mathsf{LSA}}$. This leads the calculations of the second derivates to rely on an ever smaller number of pixels, and thus to become increasingly sensitive to sensor noise which propagates to the final displacement and strain maps. An increasing value of the measurement resolution should reflect this. In addition, the preceding results were obtained for a value of $\widetilde{\ell}_{\mathsf{LSA}}$ fixed to $\widetilde{\ell}_{\mathsf{LSA}} = \frac{\sqrt{2}}{2} \times 1.4$ while this quantity can also continuously change, and changing this quantity also influences both the spatial resolution and the measurement resolution. The objective now is to see how these two parameters, namely $\widetilde{\ell}_{\mathsf{LSA}}$ on the one hand, and the $\frac{\widetilde{\ell}_{\mathsf{Hess}}}{\widetilde{\ell}_{\mathsf{LSA}}}$ ratio on the other hand, should be combined to reach the best metrological performance. The latter can be estimated by considering separately the normalized spatial resolution $\frac{1}{\widetilde{f}_{c(-10\%)}}$ and the measurement resolution, but both quantities can also be combined to form $\widetilde{\mathrm{MEI}}$. The lowest value of this quantity should ideally be obtained to reflect the best possible global metrological performance.

A second simulation was therefore performed for various values of $\widetilde{\ell}_{\mathsf{Hess}}$ and $\widetilde{\ell}_{\mathsf{LSA}}$. For each value of $\widetilde{\ell}_{\mathsf{LSA}}$, the $\frac{\widetilde{\ell}_{\mathsf{Hess}}}{\widetilde{\ell}_{\mathsf{LSA}}}$ ratio increased from 0.60 to 1.00 [-], with a step equal to 0.02 [-]. $\widetilde{\ell}_{\mathsf{LSA}}$ also increased from $\frac{\sqrt{2}}{2}$ [-] to $3 \times \frac{\sqrt{2}}{2}$ [-], with

a step equal to $0.1 \times \frac{\sqrt{2}}{2}$ [-]. The displacement resolution and the normalized spatial resolution were then estimated for each pair of $\widetilde{\ell}_{\mathsf{LSA}}$ and $\frac{\widetilde{\ell}_{\mathsf{Hess}}}{\widetilde{\ell}_{\mathsf{LSA}}}$ values, by considering, in turn, noiseless and noisy pairs of images. As for the preceding simulations, ρ was arbitrarily fixed to 6.3 [px/period], but we will see latter in this paper (Section 6) that the optimal $\frac{\widetilde{\ell}_{\mathsf{Hess}}}{\widetilde{\ell}_{\mathsf{LSA}}}$ ratio does not depend on ρ.

In the preceding section, two regimes could be distinguished concerning the shape of the curve obtained when plotting the cross-section of the displacement field along Δ. For each combination of the parameters, the spatial resolution was found by automatically detecting the intersection point of the curve and the horizontal line representing $\lambda = -10\%$. However, this may potentially lead to a value of λ greater than $\lambda = +10\%$ when Regime A is reached, thus for the lowest values of $\widetilde{\ell}_{\mathsf{Hess}}$. The corresponding cases were therefore discarded from the selection of the optimal ratio.

The influence of both $\widetilde{\ell}_{\mathsf{LSA}}$ and the $\frac{\widetilde{\ell}_{\mathsf{Hess}}}{\widetilde{\ell}_{\mathsf{LSA}}}$ ratio on the metrological performance after deconvolution is illustrated in Figure 6, ρ being fixed to 6.3 [px/period].

Figure 6 (a) first shows the displacement resolution σ_u (see definition in the Appendix) as a function of $\widetilde{\ell}_{\mathsf{LSA}}$ and $\frac{\widetilde{\ell}_{\mathsf{Hess}}}{\widetilde{\ell}_{\mathsf{LSA}}}$. It can be observed that σ_u is a decreasing function of both these quantities. This is logical since both are linked to the number of pixels covered by the Gaussian or the Mexican hat windows, thus increasing either quantity causes the number of pixels used to perform each calculation to increase. This progressively smoothes out the noise. Thus σ_u decreases.

The normalized spatial resolution $\frac{1}{\widetilde{f}_{c(-10\%)}}$ is depicted in Figure 6 (b). Contrary to σ_u, $\frac{1}{\widetilde{f}_{c(-10\%)}}$ is an increasing function of both $\widetilde{\ell}_{\mathsf{LSA}}$ and $\frac{\widetilde{\ell}_{\mathsf{Hess}}}{\widetilde{\ell}_{\mathsf{LSA}}}$. This is logical since the curves obtained along the midline Δ are shifted toward the right as either quantity increases. The values obtained for Regime A and for a vertical coordinate of the summit of the curve discussed in Section 5 greater than 10% are highlighted. It can be seen that this is the case for the last three smallest values of $\frac{\widetilde{\ell}_{\mathsf{Hess}}}{\widetilde{\ell}_{\mathsf{LSA}}}$.

Figure 6 (c) shows the value of $\widetilde{\mathrm{MEI}}$ as a function of $\widetilde{\ell}_{\mathsf{LSA}}$ and the $\frac{\widetilde{\ell}_{\mathsf{Hess}}}{\widetilde{\ell}_{\mathsf{LSA}}}$ ratio. This is the point-by-point product of the two preceding distributions. The most striking conclusion is that the value of $\widetilde{\mathrm{MEI}}$ obtained after deconvolution does not depend on $\widetilde{\ell}_{\mathsf{LSA}}$ since the plot of $\widetilde{\mathrm{MEI}}$ is invariant with respect to a translation along the $\widetilde{\ell}_{\mathsf{LSA}}$ axis. This result was demonstrated for LSA before deconvolution in [4], but it can be seen here that it remains valid after deconvolution. Another interesting result is that for a fixed value of $\widetilde{\ell}_{\mathsf{LSA}}$, decreasing the $\frac{\widetilde{\ell}_{\mathsf{Hess}}}{\widetilde{\ell}_{\mathsf{LSA}}}$ ratio (thus $\widetilde{\ell}_{\mathsf{Hess}}$) reduces (thus improves) $\widetilde{\mathrm{MEI}}$ up to a certain value beyond which it increases.

The points corresponding to the cases for which Regime A is reached and $\lambda > 10\%$ are highlighted in Figure 6 (c). It is worth noting that this minimum

value of $\widetilde{\text{MEI}}$ is obtained in the last case for which a value of λ lower than 10% is obtained. Refining these simulations with intermediate values of the $\frac{\widetilde{\ell}_{\text{Hess}}}{\widetilde{\ell}_{\text{LSA}}}$ ratio leads to an ultimate value of 0.67 for $\rho = 6.3$ [px/period]. This value is slightly greater than the value for which the summit of the curve is obtained in Figure 5 (b), which means that the optimal value of the $\frac{\widetilde{\ell}_{\text{Hess}}}{\widetilde{\ell}_{\text{LSA}}}$ ratio corresponds to λ lower than $\lambda = +10\%$. Indeed, the corresponding value is $\lambda = +4.4\%$.

5 Changing the shape of the analysis window

The main benefit of deconvolution is to improve the spatial resolution while the measurement resolution is impaired in a lower proportion. However, the spatial resolution is directly governed by the size of the analysis window since the larger this window, the higher (thus the worst) the spatial resolution. As suggested in [15], we employed in this study Gaussian analysis windows, the minimum value of the standard deviation being equal to $\widetilde{\ell}_{\text{LSA}} = \frac{\sqrt{2}}{2}$. If the goal is to obtain small details in a strain map, for instance, the reader may wonder why an analysis window sharper than this smallest Gaussian window is not directly used. Indeed, regardless of the impact on the noise level, this would automatically improve the spatial resolution without performing deconvolution.Triangular or bitriangular windows are potentially sharper than the smallest Gaussian windows employed in this study. They have been used for a long time with 2D-grids, [26–29] for instance, generally with the lines of the 2D grids aligned with the boundaries of the images. Using a checkerboard instead of 2D grids improves the contrast in the images, and thus reduces the noise level in the final maps [11]. Non-alignment of the periodic pattern with the borders prevents the images from aliasing if a suitable tilt angle is employed [17]. The effect of the shape of the analysis window on the quality of the results is discussed in Ref. [15], and the main conclusion is that the Gaussian window offers the best tradeoff between various constraints. In particular, it is shown that analysis windows sharper than a Gaussian window such as bitriangles may potentially cause harmonics to appear and disturb the phase distribution if non-integer values of the sampling density are employed. However, this conclusion was drawn from results obtained with 2D grids aligned with the boundaries of the images. To the best of the authors' knowledge, no result with windows other than the Gaussian window is presented in the literature when tilted checkerboard images are processed, so this point is briefly illustrated with an example in this section.

We consider here the case of a bitriangular window, see Figure 2 (c). Its width is equal to twice the period of the checkerboard along its diagonal. Comparing windows represented in Figure 2 (a) and (c) shows that the latter is much sharper than the former. In Ref. [15], it is shown that the width of such a bitriangular window should be a multiple of the period of the periodic pattern to prevent spurious fluctuations caused by harmonics to appear in the strain fields. With tilted checkerboard patterns and a non-integer number of pixels per period, it is however clear that this condition cannot be satisfied.

Figure 7 (a) shows the displacement field obtained by using this type of bitriangular window. A sampling density ρ equal to $\rho = 9.3$ [px/period] is employed here. The overall appearance is similar to the reference one displayed in Figure 3. Enlarging this map however shows that data are missing at places periodically placed on the map, see Figure 7 (c), which is speckled with dots. This phenomenon is caused by the phase map which is affected by a "periodic noise". This is also clearly visible in Figure 7 (b), which represents the cross-section of the displacement field along Δ. Harmonics likely causes these periodic fluctuations in the phase distribution, the effect of which is clearly visible in Figure 7 (d). A similar phenomenon was observed in the phase maps shown in Ref. [15]. Phase derivatives become too high at these places. The consequence is that the condition given by Equation 3 is no longer satisfied, and this causes the fixed-point algorithm used to calculate the displacement to diverge at these places.

This phenomenon is illustrated here with a sampling density ρ equal to $\rho = 9.3$ [px/period], lower values such as 6.3 [px/period] leading to results even more corrupted by these periodic fluctuations. This brief illustration of the use of a bitriangular window emphasizes the relevancy of employing a Gaussian window to extract the phases, and to deconvolve these maps to improve the spatial resolution without being affected by any negative impact of harmonics. In addition, the Gaussian window is isotropic, while the bitriangular one shall be aligned with the directions of the lines of diamonds forming the periodic pattern processed by LSA.

6 Influence of the sampling density ρ

So far, the sampling density ρ was considered as fixed. The goal of this section is to assess its influence on the metrological performance.

6.1 Invariance of the spatial resolution

We examine here the influence of the sampling density ρ on the results found above, with $\rho \in \{5.3, 6.3, \cdots, 11.3, 12.3\}$ [px/period]. Figure 8 shows the results found in these eight cases by plotting the cross-section along Δ of the displacement fields found before and after deconvolution. We considered here the two bounds that were taken in the calculations above for optimizing the $\frac{\widetilde{\ell}_{\mathsf{Hess}}}{\widetilde{\ell}_{\mathsf{LSA}}}$ ratio, namely 0.60 and 1.00 [-], as well as 0.67, which is the optimal value for this ratio. The coordinate along the horizontal axis is the normalized period $\widetilde{p}_{wave} = \frac{p_{wave}}{\rho}$ of the sine wave used for the reference displacement field along x_2. As mentioned in Section 2.5, the amplitude reported along the vertical axis is already normalized with respect to ρ. Considering normalized quantities enables us to fairly compare the results obtained for these eight different sampling values. The main remark is that the curves plotted in Figure 8 only shrink along the horizontal axis as the value of ρ increases. The eight curves in each of the four sets ($\frac{\widetilde{\ell}_{\mathsf{Hess}}}{\widetilde{\ell}_{\mathsf{LSA}}} = 0.60, 0.67, 1.00$ and the no-deconvolution case)

are nearly superposed. Only the height of the spike observed for $\frac{\widetilde{\ell}_{\mathsf{Hess}}}{\widetilde{\ell}_{\mathsf{LSA}}} = 0.60$ and $\frac{\widetilde{\ell}_{\mathsf{Hess}}}{\widetilde{\ell}_{\mathsf{LSA}}} = 0.67$ changes, in the case $\rho = 5.3$ [px/period] and, to a much lesser extent, in the case $\rho = 6.3$ [px/period]. It means that over the range of $\widetilde{\ell}_{\mathsf{LSA}}$ values considered here, the sampling density only marginally influences the quality of the results as long as noiseless data are considered.

6.2 Influence of ρ on σ_u and $\widetilde{\mathrm{MEI}}$

The spatial resolution is one of the metrological parameters for characterizing full-field measurements. The metrological performance must however be assessed in terms of compromise between measurement resolution and spatial resolution. The normalized value of the MEI ($\widetilde{\mathrm{MEI}}$) already discussed above is considered for this purpose. Three cases are considered for the sake of simplicity, namely $\rho = 6.3, 9.3$, and 12.3 [px/period]. Figure 9 shows the distribution of this quantity as a function of $\frac{\widetilde{\ell}_{\mathsf{Hess}}}{\widetilde{\ell}_{\mathsf{LSA}}}$ and $\widetilde{\ell}_{\mathsf{LSA}}$. The main conclusion is that the general shape of the three distributions is the same. In particular :

1. In each of the three values of ρ, $\widetilde{\mathrm{MEI}}$ does not depend on the value of $\widetilde{\ell}_{\mathsf{LSA}}$ whatever the value of ρ.
2. For any given value of $\widetilde{\ell}_{\mathsf{LSA}}$, the location of the minimum of $\widetilde{\mathrm{MEI}}$ is not influenced by ρ, which means that the optimal values of $\frac{\widetilde{\ell}_{\mathsf{Hess}}}{\widetilde{\ell}_{\mathsf{LSA}}}$ given in Section 4.2 remains valid for any acceptable value of $\widetilde{\ell}_{\mathsf{LSA}}$.
3. For $\rho = 12.3$ [px/period], the value of $\widetilde{\mathrm{MEI}}$ is missing for the highest values of both $\widetilde{\ell}_{\mathsf{LSA}}$ and the $\frac{\widetilde{\ell}_{\mathsf{Hess}}}{\widetilde{\ell}_{\mathsf{LSA}}}$ ratio. This is due to the fact that the curves obtained when plotting the cross-section of the displacement field along Δ are progressively shifted toward the right as any of these two quantities increases. The consequence is that no intersection point with the red horizontal line characterizing $\lambda = -10\%$ (see Figure 4) can be found beyond a certain value of $\widetilde{\ell}_{\mathsf{LSA}}$ and/or $\frac{\widetilde{\ell}_{\mathsf{Hess}}}{\widetilde{\ell}_{\mathsf{LSA}}}$. These points are actually outside the reference displacement field represented in Figure 3. Extending this displacement field toward the right (thus for greater values of $\widetilde{p}_{wave}$) by generating longer synthetic checkerboard images would give the possibility of finding such intersection points.
4. The only real difference between the three cases is the value of $\widetilde{\mathrm{MEI}}$. Indeed, $\widetilde{\mathrm{MEI}}$ decreases as ρ increases. This can be explained by the fact that $\widetilde{\mathrm{MEI}}$ is defined by the product of σ_u and $\frac{1}{\widetilde{f}_{c(-10\%)}}$. As mentioned above, the latter quantity is not influenced by ρ. On the other hand, the former is sensitive to this parameter. Indeed, increasing the number of pixels/period means that the number of pixels beneath the analysis window used in LSA increases as $\widetilde{\ell}_{LSA}$ increases since the physical size of this window is linked to the physical size of the period of the checkerboard. Hence, the influence of sensor noise automatically decreases as ρ increases, and so the measurement

resolution σ_u. Note that this improvement of $\widetilde{\text{MEI}}$ as ρ increases is counterbalanced by the fact that the field of view becomes smaller in proportion. This improvement is discussed in the following section for the optimal value of the $\frac{\widetilde{\ell}_{\text{Hess}}}{\widetilde{\ell}_{\text{LSA}}}$ ratio.

6.3 Conclusion

The optimized value of the $\frac{\widetilde{\ell}_{\text{Hess}}}{\widetilde{\ell}_{\text{LSA}}}$ ratio has been determined. The objective of the following section is to quantify the improvement that is achieved when using this optimized ratio in the deconvolution process, in particular in terms of spatial resolution since a simple predictive formula will be proposed to estimate this quantity.

7 Quantifying the improvement brought by deconvolution with optimal settings

The objective here is to quantify the improvement brought by deconvolution with optimal settings. We propose first a closed-form expression giving the value of the spatial resolution $\frac{1}{\widetilde{f}_{c(-10\%)}}$ after deconvolution as a function of the size of the analysis window chosen by the user to process the images with LSA, which enables us to assess the improvement of this metrological parameter after deconvolution. Noise is then taken into account and the improvement in terms of $\widetilde{\text{MEI}}$ is given. We finally assess this improvement by using an estimator widely used in the DIC community, namely the optical residual.

7.1 Closed-form expression of the spatial resolution before deconvolution

The theoretical value of $\frac{1}{f_{c(\lambda)}}$ before deconvolution can be obtained by using the transfer function of the Gaussian analysis window used in LSA. Indeed, the transfer function of any linear filter is equal to the Fourier transform of its impulse response. $\mathcal{F}(w_{\text{LSA}})$ being the continuous Fourier transform of the analysis window w_{LSA} defined in Equation 5, we have

$$\mathcal{F}(w_{\text{LSA}})(f\cos\theta, f\sin\theta) = e^{-2\pi^2\ell_{\text{LSA}}^2 f^2} \tag{17}$$

where θ defines the direction along which the phase is extracted.

For a given and necessarily negative value of λ, the cutoff frequency satisfies $e^{-2\pi^2\ell_{\text{LSA}}^2 f_{c(\lambda)}^2} = 1+\lambda$. Thus, the spatial resolution, which is defined by its inverse, reads as follows:

$$\frac{1}{f_{c(\lambda\%)}} = \pi\sqrt{\frac{-2}{\log(1+\lambda)}} \times \ell_{\text{LSA}}, \quad \lambda < 0 \tag{18}$$

Normalizing both the spatial resolution (hence the cutoff frequency) and the standard deviation of the Gaussian analysis window with respect to ρ and substituting λ by -10%, we have

$$\frac{1}{\widetilde{f}_{c(-10\%)}} = \pi\sqrt{\frac{-2}{\log(0.9)}} \times \widetilde{\ell}_{\mathsf{LSA}} \tag{19}$$

$$\simeq 13.69 \times \widetilde{\ell}_{\mathsf{LSA}} \tag{20}$$

which shows that $\frac{1}{\widetilde{f}_{c(-10\%)}}$ is proportional to $\widetilde{\ell}_{\mathsf{LSA}}$. This remark also holds for the corresponding non-normalized quantities linked through Equation 18.

7.2 Comparison with the results deduced from the synthetic images

The values of $\frac{1}{\widetilde{f}_{c(-10\%)}}$ obtained with Equation 20 are reported in Figure 10 (black diamonds) for $\widetilde{\ell}_{\mathsf{LSA}} \in \{1.0 \times \frac{\sqrt{2}}{2}, 1.1 \times \frac{\sqrt{2}}{2}, \cdots, 2.9 \times \frac{\sqrt{2}}{2}, 3.0 \times \frac{\sqrt{2}}{2}\}$. The values of $\frac{1}{\widetilde{f}_{c(-10\%)}}$ deduced from the curves (i. e. from the cross-sections of the displacement fields along Δ defined in Figure 3) are also plotted in this figure, see the small circles featuring various shades of blue. Various sampling densities ρ were considered in the synthetic images. However, the results obtained from one value of ρ to another can directly be compared since the spatial resolution $\frac{1}{\widetilde{f}_{c(-10\%)}}$ is normalized with respect to ρ. The results being line fitted and the number of points deduced from the curves decreasing as ρ increases (because the intersection point between the cross-section of the displacement filed along Δ and the horizontal line $\lambda = -10\%$ is outside the figure as $\widetilde{\ell}_{\mathsf{LSA}}$ increases), only the cases $\rho \in \{5.3, 6.3, 7.3, 8.3, 9.3\}$ [px/period] were considered here.

Line fitting gives a negligible value for the intercept (1.85E-03 [-]), so it is not taken into account. Consequently and as expected, $\frac{1}{\widetilde{f}_{c(-10\%)}}$ is directly proportional to $\widetilde{\ell}_{\mathsf{LSA}}$. In Figure 10, the relative difference between the theoretical value given by Equation 20 (black diamonds) and from the curves (blue triangles) is quite small. The slope of the line giving $\frac{1}{\widetilde{f}_{c(-10\%)}}$ as a function of $\widetilde{\ell}_{\mathsf{LSA}}$ is equal to 13.69 according to Equation 20, while line fitting the results obtained from the curves for all the values of $\rho \in \{5.3, 6.3, 7.3, 8.3, 9.3\}$ [px/period] gives 13.03, thus a 5 % relative difference. Bearing in mind the number of calculations needed to obtain the blue points, namely rendering pairs of synthetic reference/deformed images with as little bias as possible, extracting the displacement maps from these images, and deducing the spatial resolution from the curves obtained in each case, the relative difference between the two slopes seems reasonable.

The results found after deconvolution lead to the set of small triangles plotted in various shades of red in Figure 10. The points are plotted for the optimal

value of the $\frac{\widetilde{\ell}_{\mathsf{Hess}}}{\widetilde{\ell}_{\mathsf{LSA}}}$ ratio found in Section 4.2, namely $\frac{\widetilde{\ell}_{\mathsf{Hess}}}{\widetilde{\ell}_{\mathsf{LSA}}} = 0.67$. Interestingly, these points are also aligned. A complete set of 21 red triangles is available for each value of ρ, which was not the case for the circles. Indeed, the curves representing the displacement after deconvolution along Δ are much steeper than before deconvolution, so the spatial resolution deduced from these curves could be found for all the 21 values of $\widetilde{\ell}_{\mathsf{LSA}}$ considered here.

Line fitting the results gives the slope and the intercept in each case. The intercept being small (highest amplitude: 1.6E-03 [-]), it is neglected, which causes again the spatial resolution $\frac{1}{\widetilde{f}_{c(-10\%)}}$ to be proportional to $\widetilde{\ell}_{\mathsf{LSA}}$. The slope of the red lines is equal to 3.54 [-] on average.

In conclusion, and considering the value found with line fitting in the "before deconvolution" case for the sake of consistency, we have:

$$\textbf{Before deconvolution:}\quad \frac{1}{\widetilde{f}_{c(-10\%)}} \simeq 13.03 \times \widetilde{\ell}_{\mathsf{LSA}} \tag{21}$$

$$\textbf{After deconvolution:}\quad \frac{1}{\widetilde{f}_{c(-10\%)}} \simeq 3.54 \times \widetilde{\ell}_{\mathsf{LSA}} \tag{22}$$

Combining the results obtained before and after deconvolution leads to an improvement of the spatial resolution by a factor equal to $13.03/3.54 \simeq 3.68$ [-]. Both $\frac{1}{\widetilde{f}_{c(-10\%)}}$ and $\widetilde{\ell}_{\mathsf{LSA}}$ being dimensionless, their corresponding values in [px] are obtained by multiplying them by the value of ρ observed in the experiment, and eventually in [m] by multiplying this last quantity by the physical size of a pixel after projection on the specimen under study.

Reducing the value of $\widetilde{\ell}_{\mathsf{LSA}}$ improves the spatial resolution even before deconvolution, but the noise level (thus σ_u) increases. In the same spirit as for the spatial resolution, we calculated the ratio between σ_u after and before deconvolution for the optimal value of the $\frac{\widetilde{\ell}_{\mathsf{Hess}}}{\widetilde{\ell}_{\mathsf{LSA}}}$ ratio (equal to 0.67). Figure 11 is the probability distribution of this ratio estimated with the set of 8 different values of ρ and, for each of these values, 21 values of $\widetilde{\ell}_{\mathsf{LSA}}$. The noise level is multiplied by 2.02 on average, but the spatial resolution is divided by a ratio equal to 3.68, as discussed just above. This gives on average a reduction of $\widetilde{\mathrm{MEI}}$ by a factor $3.68/2.02 = 1.82$. This is reflected by calculating point-wise the ratio between the values of $\widetilde{\mathrm{MEI}}$ before and after deconvolution reported in Figure 12. Only the points for which the normalized spatial resolution $\frac{1}{\widetilde{f}_{c(-10\%)}}$ could be determined from the curves are shown in this figure. This ratio should be equal, on average, to $1/1.82 = 0.549$, while the mean value of the values represented in Figure 12 is equal to 0.547, which is very close.

7.3 Impact of deconvolution on the optical residual

The readers being certainly accustomed to the use of DIC, we examine here how deconvolution impacts the optical residual estimated with the synthetic

reference and deformed checkerboard images. The latter is obtained by deforming the reference image through the reference displacement field defined in Section 2.2. These images considered here are those obtained in the typical case $\rho = 6.3$ [px/period].

The optical residual is often used to assess the metrological performance of DIC [30–32]. It is obtained by calculating the difference in gray level at each pixel between the reference image, and the deformed image corrected by the displacement field measured. To obtain this latter image, an interpolation of the gray level is necessary, since the displacement is usually not an integer. This interpolation is often performed with spline functions, which are considered to be optimal since they lead to the lowest interpolation errors, as reported in [33]. This method was thus used in the present study. Four displacement fields were considered here to deform the reference image and calculate the optical residual:

1. The displacement field obtained with LSA without deconvolution, with $\widetilde{\ell}_{\mathsf{LSA}} = 1$ [-].
2. The displacement field obtained with LSA with deconvolution, with $\widetilde{\ell}_{\mathsf{LSA}} = 1$ [-] and $\frac{\widetilde{\ell}_{\mathsf{Hess}}}{\widetilde{\ell}_{\mathsf{LSA}}}$=1.0 [-].
3. The displacement field obtained with LSA with deconvolution, with $\widetilde{\ell}_{\mathsf{LSA}} = 1$ [-] and $\frac{\widetilde{\ell}_{\mathsf{Hess}}}{\widetilde{\ell}_{\mathsf{LSA}}}$=0.67 [-].
4. The reference displacement field defined in Section 2.2.

The second case corresponds to a typical deconvolution for which the value of the $\frac{\widetilde{\ell}_{\mathsf{Hess}}}{\widetilde{\ell}_{\mathsf{LSA}}}$ ratio is not optimal, whereas this ratio is optimal in the third case since $\frac{\widetilde{\ell}_{\mathsf{Hess}}}{\widetilde{\ell}_{\mathsf{LSA}}} = 0.67$. In Figure 13, the standard deviation of the residual is calculated columnwise. This quantity is denoted by $\sigma_{residual}$. Noisy images were used here, so $\sigma_{residual}$ was normalized in each case with respect to σ_{image}, which is the standard deviation of image noise estimated over the whole image. This normalization step is common in studies dealing with the metrological performance of DIC [34, 35] for instance, since it leads to a "perfect target value" equals to $\frac{\sigma_{residual}}{\sigma_{image}} = 1.00$, which is independent of the noise level. The results obtained for the first three cases listed above are plotted in different shades of blue for the first three displacement fields. The normalized standard deviation obtained with the residual estimated with the reference displacement field is also plotted in red. Both the horizontal displacement u_1 and the vertical displacement u_2 were considered in the four different cases to compute the residual, even though the amplitude of the horizontal displacement is much lower than the amplitude of the vertical one for the first three cases (the reference displacement along x_1 is rigorously null in the last case). Several conclusions can be drawn from the results shown in this figure:

- The highest normalized standard deviation is obtained with the raw displacement field returned by LSA (*i.e.* without deconvolution), successively followed by the displacement field obtained with deconvolution using the

non-optimal $\frac{\widetilde{\ell}_{\mathsf{Hess}}}{\widetilde{\ell}_{\mathsf{LSA}}}$ ratio, and by its counterpart obtained with the optimal ratio equal to 0.67. This conclusion is consistent with the ranking obtained in terms of spatial resolution or normalized MEI.

- The normalized value of the residual is nearly the same in all cases for the highest values of $\widetilde{p}_{wave}$. On close inspection (by considering a close-up view of these curves on the right-hand side, not shown here), the residual obtained with the reference displacement field is always lower than the three others.
- Interestingly, the residual increases on the left (towards the high spatial frequencies) even with the reference displacement field. One of the causes is certainly interpolation. Indeed, it becomes progressively difficult to correctly interpolate the gray level distribution as the spatial frequency of the displacement increases. It is worth noting that image gradient is significant in checkerboard images, which makes it difficult to properly reconstruct the gray level by interpolation in case of high-frequency displacements.
- The normalized spatial resolution $\frac{1}{\widetilde{f}_{c(-10\%)}}$ estimated with the first three displacement fields is also reported in this figure. The spatial resolution and the residual are correlated since the lower the former, the lower the value of $\widetilde{p}_{wave}$ for which the curve straightens, which seems logical.
- The value of the normalized residual is by definition greater than one. Its order of magnitude is close to one on the right and progressively increases when going to the left, thus when the spatial frequency of the displacement increases. Depending on the test case, a successful image analysis can be considered with normalized residuals ranging from 1 to 3 [34, 35]. As seen in Figure 13, this must be weighted in some cases, *e.g.* in case of high-frequency displacements. Over the range of $\widetilde{p}_{wave}$ values for which deconvolution notably improves the raw displacement returned by LSA, say between the spatial resolution of LSA before ($\frac{1}{\widetilde{f}_{c(-10\%)}} = 12.80$ [−]) and after ($\frac{1}{\widetilde{f}_{c(-10\%)}} = 3.47$[−]) deconvolution with optimal settings, it is worth noting that the normalized residual lies between 1.06 and 2.64 [-], which is consistent with the values of this residual for which the displacement found with the measurement technique can be considered as of good quality.
- Some singular results are observed in the four curves for $\widetilde{p}_{wave} \simeq 6$[-]. This is due to an interplay, for a given wave period, between the periodic pattern and the periodic vertical displacement field.
- Only the normalized standard deviation of the residual estimated columnwise is represented and discussed here. Indeed, it is worth noting that plotting the Root Mean Square Error gives exactly the same type of curves, which means that no bias impacts the results

8 Application to real images

Before closing the paper, we illustrate the benefit of using on real images the deconvolution procedure with optimized settings. Two different examples are considered. The first one is a disk made of a single crystal of shape

memory alloy (SMA). It is subjected to a cooling which induces an austenite-to-martensite phase transformation. Both phases coexist, with sharp interfaces inbetween. "Sharp" means that a strain jump theoretically occurs from one phase to another. It also means that the border between these two phases goes through the analysis window when processing the images, which makes it challenging to return a reliable strain value in the corresponding small zones. The second example deals with a wood specimen subjected to a tensile test. Heterogeneities in the strain field are caused here by the presence of annual rings and by a knot embedded in the tensile specimen. Compared to the preceding example, the strain level is globally much lower, which decreases the signal-to-noise ratio. The heterogeneities are also less marked than in the preceding case. The optimal value for the $\frac{\widetilde{\ell}_{\mathsf{Hess}}}{\widetilde{\ell}_{\mathsf{LSA}}}$ defined in Section 4.2 is chosen for finding all the strain distributions discussed in these two examples.

8.1 Shape memory alloy specimen

As discussed in a recent review paper [36], there is a wide literature on the use of full-field measurement techniques to study the peculiar thermomechanical properties of shape memory alloys, [37–41] for instance. We show with this example that using optimized checkerboard patterns, LSA, and deconvolution leads to a detailed strain map enabling to highlight the microstructures underlying these properties.

The specimen considered here is a 33 mm in diameter, 3 mm thick disk made of a single crystal of $CuAl_{13.9}Ni_{4.6}$ (wt%) SMA. The chemical composition was chosen to allow for full austenite (A) state to be observed at room temperature (approximately equal to 23° C). This is the reference state for the strain measurements shown and discussed below. The specimen was placed on a Pelter cell and cooled, so the martensite (M) phase appeared without any external mechanical load. The A→M transformation manifests itself here by the appearance of martensitic microstructures, which involve different variants of martensite. The same strain tensor takes place in all these variants, but its orientation with respect to the (parent) austenite phase changes from one variant to another. The A→M phase transformation was therefore tracked by its impact on the strain maps measured on the surface of the specimen. These strain maps were obtained by preliminary depositing a checkerboard pattern on one of the two surfaces of the specimen considered in the austenite state. The nominal period p of this periodic pattern was 60 microns, see Figure 14. Full details on the patterning technique, which relies on laser marking, are given in [42]. Three circles are superposed to this figure. The red one is, according to the "3-σ rule" [16], the apparent size of the Gaussian analysis window used in LSA. The diameter of the blue circle is equal to the spatial resolution $\frac{1}{f_{c(-10\%)}}$ before deconvolution. The diameter of the green circle is also equal to the spatial resolution, but after deconvolution, so it is smaller than the blue one. It can be observed that the green circle is smaller than the apparent size of the Gaussian analysis window.

This patterned surface was filmed by a Prosilica GT 6600 camera featuring a CCD sensor of size $6576 \times 4384 \simeq 28.8\text{E+}06$ [px], with a gray depth equal to 256 [bits]. The shutter time was equal to 8 [ms], and the number of frames per second to one. In the checkerboard images, the sampling density was $\rho = 8.2$ [px/period]. This camera was equipped with a telecentric lens. The images shot during the test were processed by using the LSA procedure described in Section 2.1 above, and deconvolution was applied to the phase maps to sharpen fine details in the strain maps that revealed the appearance and evolution of the microstructures during the tests. A complete discussion of the results found during this experiment will be available in a separate paper. We only give here one of the numerous maps which were obtained, and illustrate the benefit, in terms of detail sharpening, of using the deconvolution procedure with optimized settings.

Figure 15 shows a typical U_{12} map before and after deconvolution. This is one of the components of the right stretch tensor denoted by $\underline{\underline{U}}$, this latter quantity being more suitable than the linearized strain tensor $\underline{\underline{\varepsilon}}$ to study microstructures in SMAs. Figure 15 (a) is the raw output of the LSA procedure, employed here with a Gaussian window set with $\widetilde{\ell}_{\mathsf{LSA}} = \frac{\sqrt{2}}{2}$ [-]. The reader is invited to zoom in the electronic version of the paper in order to appreciate the details. Indeed, the strain resolution for this measurement technique is typically some 10^{-4} [-], and since the strain to be measured is equal to some 10^{-2} [-], the signal-to-noise ratio is here quite favorable. $\widetilde{\ell}_{\mathsf{LSA}}$ was therefore chosen to be equal to its lowest possible value in order to boost the ability of the technique to reveal the smallest possible details. The size of both the raw and the deconvolved maps is $4384 \times 4592 \simeq 20.13\text{E+}06$ [px], among which 15.64E+06 [px] correspond to the surface of the specimen. The diameter of the red circle in Figure 14 is equal to $8.16 \times 6 \times \frac{\sqrt{2}}{2} \simeq 255$ [microns]. It means that the strain maps were obtained with 15.64 millions of disk-shaped strain gages, each of them having a diameter of 255 [microns] and being shifted by one pixel $=60/8.16 \simeq 7.35$ [microns] from one another. There is therefore a strong overlap between these disks, which causes the blur in the raw strain maps to occur. The idea is therefore to observe here to what extent deconvolution limits this blur. Obtaining with LSA the in-plane components of the right stretch tensor took 61 [s] with a computer equipped with an Intel 8-core, i9-11950H @ 2.60Ghz. Deconvolution being more time-consuming, 744 [s] were necessary to obtain the deconvolved components of the right stretch tensor.

The improvement brought by deconvolution is not readily apparent when comparing Figures 15 (a) and (b), but Figure 15 (c) shows that a difference exists. Two small zones were first chosen and enlarged to observe the change caused by deconvolution clearly. They are represented by the blue and red rectangles, respectively. These enlargements are represented in Figures 16 and 17, respectively. Figures 16 (a) and (b) clearly show over the red rectangle that the maps are sharper and more defined after deconvolution, with small details becoming visible. The same circles as those plotted in Figure 14 are superposed in Figure 16 (a) (blue circle) and 16 (b) (green circle), so that

the reader can easily compare their size with the size of the sharp details in the strain distribution. The cross-section of the U_{12} distribution shown in Figures 16 (d) is obtained along the black arrow superposed to the maps shown in Figures 16 (a), (b) and (c). It is clear that the peaks and valleys become sharper after deconvolution, as expected.

We can check the consistency of the results found here with those discussed in Section 4.2 with the reference displacement field. Indeed, we are here in a case for which the strain distribution in Figure 16 (d) is wave-like, locally dominated by a portion of sine with a certain period. According to the conclusion of Section 2.4, we are here in a case for which the relative difference between strain after and before deconvolution is the about same as that observed on the displacement distribution. We can therefore at least check that the order of magnitude of the enhancement of the experimental strain distribution is the same as that observed in the reference displacement field for the same local period of the wave. For instance, Points B_1 and C_1 in Figure 16 (d) can be regarded as roughly forming a half sine wave with half a period equal to the difference of the abscissa between those points, and an amplitude equal to half the distance of the coordinates of these two points along the vertical axis. This amplitude measured this time on the strain distribution after deconvolution (see Points A_1 and D_1) gives another value. The relative difference between the two enables us to assess the apparent "damping" caused by convolution.

In practice, finding these quantities consists in estimating the values given by those curves after and before deconvolution, for a period equal to that estimated in Figures 16 (d) with Points B_1 and C_1 (or Points A_1 and D_1, which is the same), and in assessing from these curves to what extent the amplitude of the signal increases thanks to deconvolution. For instance, we consider the peak-to-valley values given by Points B_1-C_1 on the one hand, and by Points A_1-D_1 on the other hand. They are equal to 0.0261-(-0.0128) = 0.0389 and to 0.0312-(-0.0245) = 0.0557, respectively. The relative increase of the amplitude between the two is equal to $\frac{0.0557-0.0389}{0.0389} \simeq 43.2$ %. Considering that the value of the periodic distribution locally dominating the displacement distribution at Points A_1 to D_1 is equal to $23 \times 2 = 46$ pixels and that the period of the checkerboard is equal to 8.16 pixels/period, the value of $\widetilde{p}_{wave}$ is equal to $46/8.16 \simeq 5.64$ [-]. Reporting this value on the graphic representation of the curve deduced along Δ from the displacement field obtained from the synthetic images before and after deconvolution with $\widetilde{\ell}_{\mathsf{LSA}} = \frac{\sqrt{2}}{2}$ [-] and $\frac{\widetilde{\ell}_{\mathsf{Hess}}}{\widetilde{\ell}_{\mathsf{LSA}}} = 0.67$ [-], presented in Figure 16 (e), enables us to obtain the enhancement of the amplitude of the reference displacement field retrieved by LSA for this value of $\widetilde{p}_{wave}$. This relative increase is equal to $\frac{0.509-0.376}{0.376} \simeq 35.4$ %. This quantity is lower than the relative increase observed in the experimental strain map (43.2 %), but we only consider the sine function, which locally dominates the strain distribution. Other harmonics are potentially influential, and thus also impact the improvement brought in this case by deconvolution. In addition, this period is roughly estimated. It is indeed an integer value since the information is sampled, which also induces an approximation. Finally, any

slight fluctuation of this period strongly influences the amplitude retrieved in Figure 16-(e), since the slope of the curves representative of the amplitude before and after deconvolution for this value of $\widetilde{p}_{wave}$ is significant. We can only conclude that the order of magnitude of the enhancement brought by deconvolution is the same for both the experimental strain map and the reference displacement map for this value of $\widetilde{p}_{wave}$. The same reasoning applied on the pseudo-period defined by Points A_2-D_2-A_3 and B_2 C_2-B_3 leads to a local value of $\widetilde{p}_{wave}$ equal to 4.23 [-]. The corresponding local increase of the amplitude is equal to 58.7 % for the experimental strain map and 74.9 % for the reference displacement field at the same value of $\widetilde{p}_{wave}$. This again gives the same order of magnitude.

Figure 17 now illustrates the enhancement brought by deconvolution over the blue rectangle. Plotting the strain distribution along the black arrow for the raw and the deconvolved distributions along this line enables us to observe this enhancement, see Figure 17 (d). Compared to the preceding case, the period of the sine wave that locally approximates the strain distribution is smaller, and the correction induced by deconvolution is consequently more pronounced. For instance, the local apparent period between Points A_1 and D_1 in Figure 17 (d) is equal to 14 [px], thus the local value of $\widetilde{p}_{wave}$ is equal to $14/8.16 \simeq 1.72$ [-], which is much lower than the normalized spatial resolution after deconvolution, equal here to 2.39 [-], see Figure 16 (e). It means that even though it can be seen to the naked eye that the correction brought by deconvolution is significant, it is certainly not sufficient to reach an absolute value of λ lower than $\lambda = 10\%$.

The green rectangle represented in Figure 15 is now considered. It is free of any microstructure, so the idea is to observe here how noise changes between the raw and the deconvolved strain maps. The closeup view in Figure 18 shows that the sensor noise in the specimen images causes a spatially correlated noise in the displacement and strain maps, hence the "blobs" in the maps. This spatial correlation is quantified by the out-of-diagonal terms of the covariance matrix of this noise given in [9]. Indeed, the deconvolution procedure does not distinguish the features caused by reliable information, and those due to noise. As discussed in [23], deconvolution can be applied only to spatial frequencies lower than a certain threshold value fixed by the user. However, it can be checked that fixing this threshold value as the inverse of the value of $\widetilde{p}_{wave}$ below which LSA returns no real information, does not decrease the noise level while deconvolving the phase maps. Comparing the colorbars in Figures 18 and 17 or 16 however shows that the noise is lower in amplitude than the strain level observed in the microstructures that appear in the specimen.

8.2 Wood specimen

We consider here a parallelelipipedic wood specimen already discussed in Ref. [42], so the reader is referred to this paper for more details about the testing conditions. The presence of a knot at the center of the gage section as

well as of annual rings (see the zone of interest in Figure 19 (a)) causes heterogeneities in the strain field. Such heterogeneities are generally studied with DIC, [43–45] for instance, so the idea is to see here how LSA and deconvolution render them.

The dimensions of the specimen are $250 \times 35 \times 15$ mm^2. The checkerboard pattern was deposited on the front face of this specimen by laser marking. Its period was 100 microns, which corresponds to 6.23 pixels in the images. The images of the pattern were shot with the same camera as in the preceding example. This specimen was subjected to a tensile test along the x_1-direction. The magnitude of the load was such that the normal stress was lower than the limit of elasticity. Two main differences are noticeable compared to the preceding example:

- The strain level is much lower here since the mean value remains lower than 10^{-3} for the three in-plane strain components, with some localized peaks not higher than a few 10^{-3}. This is about ten times lower than the strain peaks reached in the SMA specimen of the first example. It means the information barely emerges from the noise floor in this second example.
- The strain field is "less heterogeneous" in the sense that the fluctuations of the strain distribution throughout the specimen are smoother.

The sharpness of the details must be evaluated with respect to the size of the analysis window. A brief comparison between various settings for the analysis window is offered below. Only the ε_{22} is discussed, but similar results and conclusions could be obtained with the other two in-plane strain components ε_{11} and ε_{12}.

We show first in Figure 19 (b) the ε_{22} strain map obtained by choosing the smallest possible value for $\widetilde{\ell}_{\mathsf{LSA}} = 1 \times \frac{\sqrt{2}}{2}$ [-]. This case is referred to as "Case 1" in the following. The heterogeneities caused by the presence of the knot and the annual rings are clearly visible. The noise level in this map is higher than in the preceding example. This is confirmed by plotting in Figure 20 the cross-section of the ε_{22} strain map along the inclined arrow superposed to this map. Indeed, fluctuations with significant amplitude affect the corresponding curve (in black in this figure). Deconvolution mainly causes here the noise level to increase without any clear improvement of the real details in the ε_{22} map (not shown here). It means that the real strain map, which remains unknown here, does not significantly activate the frequency range restored by deconvolution.

Deconvolution can however be employed to improve the quality of this measurement in a different way. Indeed, in the case of noisy maps, the standard solution to decrease the noise level consists in filtering them. The noise level decreases but the actual details too if they are too sharp. Equivalently, we can also apply LSA here with a larger analysis window. An example is given in Figure 19 (c), where $\widetilde{\ell}_{\mathsf{LSA}}$ is multiplied by a factor equal to 3.68, thus $\widetilde{\ell}_{\mathsf{LSA}} = 3.68 \times \frac{\sqrt{2}}{2}$ [-]. This case is referred to as "Case 2a" in the following. Comparing the results obtained in Cases 1 and 2a clearly show that the noise level decreases in the second case, but the details are also blurred, as can be

seen by examining the effect of the knot and the annual rings in these figures. Indeed, enlarging the analysis window by a factor k causes the displacement resolution to be reduced by the same factor, and the strain resolution by a factor $\sqrt{k}$, as discussed in [9, 13, 46]. This is visually confirmed when representing in Figure 19 (d) the difference between the results obtained in Cases 2a and 1.

Multiplying $\widetilde{\ell}_{\mathsf{LSA}}$ by a factor $k = 3.68$ causes the spatial resolution to be multiplied by a factor 3.68, but according to the discussion in Section 7.2, applying deconvolution ("Case 2b") causes the spatial resolution to be divided by the same factor. Thus, combining these two results causes the spatial resolution to be the same in both the Cases 1 and 2b. The map obtained in Case 2b is displayed in Figure 19 (e). The strain map is noisier compared to Case 2a, but the features corresponding to the knot and the annual rings are sharper than in Case 2a. Figure 19 (f) shows the difference between the strain maps obtained in Cases 1 and 2b. The features caused by the knot and the annual rings are nearly not distinguishable, which means that the actual details caused by the knot are correctly restored.

Plotting in Figure 20 the cross-section of the strain maps obtained in these different cases confirms this noise reduction when going from Case 1 to Case 2b. It is even more marked than in the strain maps directly, the eye being less sensitive to the color change corresponding to the amplitude change. The reason is certainly that the same features can be observed in Cases 2a and 2b.

In conclusion, applying deconvolution on the results obtained in Case 2a is equivalent to applying a low-pass filter on the results obtained in Case 1, but without affecting the frequencies lower than the inverse of the spatial resolution corresponding to the latter case. This is confirmed by applying the same procedure on the reference displacement map and plotting the displacement obtained in Cases 1, 2a, and 2b along Δ, see Figure 21. It can be seen that the normalized cutoff frequency is the same in Cases 2b and 1. Its inverse is equal to $\frac{1}{\widetilde{f}_{c(-10\%)}} = 9.06$ [-] in Case 1 according to Equation 21, and the same result is obtained in Case 2b with Equation 22. This spatial resolution is observed to be equal to 9.21 [-] from the curves. The difference between the two is due to the fact that the results given by Equations 21 and 22 are approximate. It is also worth noting that the frequencies greater than the cutoff frequency (which is the same in Cases 1 and 2b) are more "rapidly" damped in Case 2b.

9 Conclusion

The improvement of a deconvolution algorithm suitable for displacement and strain maps obtained with LSA was discussed in this paper. Three main conclusions can be drawn from the results which were discussed:

- The deconvolution algorithm mainly relies on the calculation of the Hessian matrix of the phase maps obtained with LSA. The corresponding second derivatives are calculated by using a second-order derivative kernel, namely a so-called "Mexican hat". The convergence of the deconvolution algorithm is ensured if the size of this derivative kernel is proportional to the size of

the Gaussian analysis kernel employed in LSA, and if the ratio between the two is within an acceptable range.

- An optimal value for the ratio between the sizes of the "Mexican hat" on the one hand, and the Gaussian analysis window on the other hand, has then been estimated. This optimal value shall be employed to achieve the lowest (thus the best) possible Metrological Efficiency Indicator (MEI), which is used here to assess the global metrological performance of the measuring technique. In addition, it has been observed that this indicator remains invariant after deconvolution as the size of the analysis window used in LSA changes. This invariance was demonstrated so far to be invariant only before deconvolution.
- Changing the sampling density with which the periodic pattern is encoded only affects the measurement resolution, thus the noise level observed in the final displacement and strain maps. The systematic error and the spatial resolution, which are consequences of the fact that LSA behaves like a low-pass filter, are not impacted by this density beyond the minimal value which is recommended for this quantity, namely approximately 5 pixels/period according to [11, 24]. Increasing the sampling density improves (thus reduces) the MEI, which is counterbalanced by the fact that the field of view diminishes

Two examples illustrate the improvement brought by deconvolution with these optimal settings. The first specimen is a disk made of shape memory alloy. Sharp microstructures appear when the specimen is thermally loaded. The second one is a parallelepipedic wood specimen where a knot is embedded. It is subjected to a tensile test. The signal-to-noise ratio is about ten times higher in the first example than in the second. The first example underlines the fact that the present measuring technique is well-suited to restore sharp details which appear in strain maps. In the second case, deconvolution is used to filter out the noise without damping the actual details up to a spatial cutoff frequency, which is higher than the one that would be obtained by directly filtering the strain maps with a smoothing kernel.

Acknowledgements

The authors acknowledge support from the ANR Grant ANR-18-CE08-0028-01. This work was also sponsored by the French government research program "Investissements d'Avenir" through the IDEX-ISITE initiative 16-IDEX-0001 (CAP 20-25), and from the AURA regional council.

Data Availability

Data will be provided on demand.

Ethics declarations/Conflict of Interest

The authors declare that they have no conflict of interest.

Appendix: metrological parameters

The metrological performance of the full-field measurement techniques discussed in this paper is estimated with four parameters, namely the measurement resolution σ_u, the matching bias, the spatial resolution and the metrological efficiency indicator. These quantities are defined as follows:

- The displacement resolution σ_u quantifies the random noise level which affects these maps. It is mainly caused by sensor noise propagation. According to [47], σ_u is equal to the standard deviation of the noise in the displacement maps.
- The systematic error (or bias) reflects that the amplitude of small details is generally lower than the real one. This change in amplitude is expressed as a percentage λ of the amplitude of a sine wave characterized by a given period p_{wave}. Thus, considering the reference displacement field of amplitude 0.5 [px] defined in Section 2.2, and denoting by "ampl" the amplitude of the sine wave returned by the measuring system for a certain period p_{wave}, we have:

$$\lambda = \frac{\text{ampl} - 0.5}{0.5} \times 100 \ [\%] \tag{23}$$

  It is worth noting that contrary to the maps returned by DIC or by LSA for which λ is negative since we have a loss of amplitude, deconvolution may return an amplitude of the signal greater than the reference one, λ becoming positive in this case.
- The spatial resolution reflects the ability of the technique to distinguish close features in a displacement/strain map. According to [48], it is defined as the period of the sine wave for which the value of λ equal to a threshold value arbitrarily fixed to -10 %, as in previous studies dealing with the metrological performance of full-field measurement techniques [4, 5, 19, 20]. The inverse of this period is referred to as the cutoff frequency. It is denoted by $f_{c(\lambda)}$. Changing the threshold value λ also changes the value of this frequency.
- These three quantities are not independent but linked. They depend in particular on some settings made arbitrarily by the user, the main one being the size over which calculations are performed around a given pixel to obtain a measurement at this pixel. With the present approach, this is the size of the analysis window used in LSA. With a Gaussian window, this size is governed by the standard deviation ℓ_{LSA}. A quantity independent of this size has been introduced in [4] to overcome this shortcoming, namely the Metrological Efficiency Indicator denoted by MEI. It is merely defined as the product between the spatial resolution and the displacement resolution. The advantage of using the MEI is that it is independent of ℓ_{LSA} before deconvolution, as discussed in [4]. The MEI is, therefore, a parameter that

is intrinsic to the technique and thus enables a fair comparison between different techniques [4, 5], or between different versions of the same techniques like DIC [19, 20]. An issue addressed in this study is to know if MEI is still independent of ℓ_{LSA} after deconvolution, and to what extent the sampling density ρ influences this quantity. These questions are addressed in Sections 4.2 and Sections 6, respectively.

Note that, in this paper, $f_{c(\lambda)}$ and MEI are normalized with respect to the sampling density of the periodic pattern denoted by ρ, see Section 2.5. The corresponding normalized quantities are denoted by $\widetilde{f_{c(\lambda)}} = f_{c(\lambda)} \times \rho$ and $\widetilde{\mathrm{MEI}} = \frac{\mathrm{MEI}}{\rho}$, respectively.

References

[1] Fayad, S.S., D.T., Seidl, Reu, P.L.: Spatial DIC errors due to pattern-induced bias and grey level discretization. Experimental Mechanics **60**(2), 249–263 (2020)

[2] G. F. Bomarito, J. D. Hochhaltera, T. J. Rugglesb, A. H. Cannon: Increasing accuracy and precision of digital image correlation through pattern optimization. Optics and Lasers in Engineering **91**(April), 73–85 (2017)

[3] Shi, Y., Blaysat, B., Chanal, H., Grédiac, M.: Introducing virtual DIC to remove interpolation bias and process optimal patterns. Experimental Mechanics **63**(4), 637–653 (2023)

[4] Grédiac, M., Blaysat, B., Sur, F.: A critical comparison of some metrological parameters characterizing local digital image correlation and grid method. Experimental Mechanics **57**(6), 871–903 (2017)

[5] Grédiac, M., Blaysat, B., Sur, F.: On the optimal pattern for displacement field measurement: random speckle and DIC, or checkerboard and LSA? Experimental Mechanics **60**(4), 509–534 (2020)

[6] Grédiac, M., Sur, F., Blaysat, B.: Comparing several spectral methods used to extract displacement and strain fields from checkerboard images. Optics and Lasers in Engineering **127**, 105984 (2020)

[7] Schreier, H.W., Sutton, M.A.: Systematic errors in digital image correlation due to undermatched subset shape functions. Experimental Mechanics **42**(3), 303–310 (2002)

[8] Schreier, H., Orteu, J.J., Sutton, M.A.: Image Correlation for Shape, Motion and Deformation Measurements: Basic Concepts, Theory and Applications, (2009). ISBN-978-0-387-78746-6

[9] Sur, F., Grédiac, M.: Towards deconvolution to enhance the grid method for in-plane strain measurement. Inverse Problems and Imaging **8**(1), 259–291 (2014)

[10] Grédiac, M., Sur, F., Badulescu, C., Mathias, J.-D.: Using deconvolution to improve the metrological performance of the grid method. Optics and Lasers in Engineering **51**(6), 716–734 (2013)

[11] Grédiac, M., Blaysat, B., Sur, F.: Extracting displacement and strain fields from checkerboard images with the localized spectrum analysis. Experimental Mechanics **59**(2), 207–218 (2019)

[12] Sur, F., Blaysat, B., Grédiac, M.: Rendering deformed speckle images with

a Boolean model. Journal of Mathematical Imaging and Vision **60**(5), 634–650 (2018)

[13] Grédiac, M., Sur, F., Blaysat, B.: The grid method for in-plane displacement and strain measurement: a review and analysis. Strain **52**(3), 205–243 (2016)

[14] Khamsi, M.A., Kirk, W.A.: An Introduction to Metric Spaces and Fixed Point Theory, (2001). Wiley

[15] Sur, F., Grédiac, M.: Influence of the analysis window on the metrological performance of the grid method. Journal of Mathematical Imaging and Vision **56**(3), 472–498 (2016)

[16] Grafarend, E.W.: Linear and Nonlinear Models: Fixed Effects, Random Effects, and Mixed Models, (2006). Walter de Gruyter. ISBN-13:978-3-11-016216-5

[17] Sur, F., Blaysat, B., Grédiac, M.: Determining displacement and strain maps immune from aliasing effect with the grid method. Optics and Lasers in Engineering **86**, 317–328 (2016)

[18] Foi, A., Trimeche, M., Katkovnik, V., K. Egiazarian, K.: Practical Poissonian-Gaussian noise modeling and fitting for single-image raw-data. IEEE Transactions on Image Processing **17**(10), 1737–1754 (2008)

[19] Reu, P.L., Blaysat, B., Andó, E., Bhattacharya, K., Couture, C., Couty, V., Deb, D., Fayad, S.S., Iadicola, M.A., Jaminion, S., Klein, M., Landauer, A.K., Lava, P., Liu, M., Luan, L.K., Olufsen, S.N., Réthoré, J., Roubin, E., Seidl, D.T., Siebert, T., Stamati, O., Toussaint, E., Turner, D., Vemulapati, C.S.R., Weikert, T., Witz, J.F., Witzel, O., Yang, J.: DIC challenge 2.0: developing images and guidelines for evaluating accuracy and resolution of 2D analyses. Experimental Mechanics **62**(1), 639–654 (2022)

[20] Blaysat, B., Neggers, J., Grédiac, M., Sur, F.: Towards criteria characterizing the metrological performance of full-field measurement techniques. application to the comparison between local and global versions of DIC. Experimental Mechanics **60**(3), 393–407 (2020)

[21] Chen, B., Coppieters, S.: Meshfree digital image correlation using element free Galerkin method: theory, algorithm and validation. Experimental Mechanics **63**(3), 517–528 (2023)

[22] Wang, Y., Zhao, J.: DIC-Net: Upgrade the performance of traditional DIC with Hermite dataset and convolution neural network. Optics and Lasers in Engineering **160**, 107278 (2023)

[23] Grédiac, M., Blaysat, B., Sur, F.: A robust-to-noise deconvolution algorithm to enhance displacement and strain maps obtained with local DIC and LSA. Experimental Mechanics **59**(2), 219–243 (2019)

[24] Qin, S., Grédiac, M., Blaysat, B., Ma, S., Sur, F.: Influence of the sampling density on the noise level in displacement and strain maps obtained by processing periodic patterns. Measurement **173**, 108570 (2021)

[25] Reu, P.: All about speckles: Aliasing. Experimental Techniques **38**(5), 1–3 (2014)

[26] Avril, S., Vautrin, A., Surrel, Y.: Grid method: Application to the characterization of cracks. Experimental Mechanics **44**(1), 37–43 (2004)

[27] Piro, J.L., Grédiac, M.: Producing and transferring low-spatial-frequency grids for measuring displacement fields with moiré and grid methods. Experimental Techniques **28**(4), 23–26 (2004)

[28] Moulart, R., Rotinat, R., Pierron, F., Lerondel, G.: On the realization of microscopic grids for local strain measurement by direct interferometric photolithography. Optics and Lasers in Engineering **45**(12), 1131–1147 (2007)

[29] Moulart, R., Pierron, F., Hallett, S.R., Wisnom, M.R.: Full-field strain measurement and identification of composites moduli at high strain rate with the virtual fields method. Experimental Mechanics **51**(4), 509–536 (2011)

[30] Mathieu, F., Hild, F., Roux, S.: Identification of a crack propagation law by digital image correlation. International Journal of Fatigue **36**(1), 146–154 (2012)

[31] Charbal, A., Dufour, J.-E., Guery, A., Hild, F., Roux, S., Vincent, L., Poncelet, M.: Integrated digital image correlation considering gray level and blur variations: Application to distortion measurements of IR camera. Optics and Lasers in Engineering **78**, 75–85 (2016)

[32] Jailin, T., Tardif, N., Chaudet, P., Desquines, J., Coret, M., Baietto, M.-C., Georgenthum, V.: Measuring both thermal and kinematic full-fields using a single CMOS camera during high temperature tests. Optics and Lasers in Engineering **158**, 107107 (2022)

[33] Keys, R.: Cubic convolution interpolation for digital image processing. IEEE transactions on acoustics, speech, and signal processing **29**(6), 1153–1160 (1981)

[34] International Digital Image Correlation Society, Jones E.M.C. and Iadicola M.A. (Eds): A good practices guide for Digital Image Correlation. https://doi.org/10.32720/idics/gpg.ed1. Online (2018)

[35] Mathieu, F., Leclerc, H., Hild, F., Roux, S.: Estimation of elastoplastic parameters via weighted FEMU and integrated-DIC. Experimental Mechanics **55**, 105–119 (2015)

[36] Delpueyo, D., Jury, A., Balandraud, X., Grédiac, M.: Applying full-field measurement techniques for the thermomechanical characterization of SMAs: a review and classification. Shape Memory and Superelasticity **7**, 462–490 (2021)

[37] Louche, H., Schlosser, P., Favier, D., Orgéas, L.: Heat source processing for localized deformation with non-constant thermal conductivity. application to superelastic tensile tests of NiTi shape memory alloys. Experimental Mechanics **52**(9), 1313–1328 (2012)

[38] Reedlunn, B., Churchill, C.B., Nelson, E.E., Shaw, J.A., Daly, S.H.: Tension, compression, and bending of superelastic shape memory alloy tubes. Journal of the Mechanics and Physics of Solids **63**, 506–537 (2014)

[39] Xiao, Y., Zeng, P., Lei, L., Du, H.: Local mechanical response of superelastic niti shape-memory alloy under uniaxial loading. Shape Memory and Superelasticity **1**(4), 468–478 (2015)

[40] Su, T.-H., Lu, N.-H., Chen, C.-H., Chen, C.-S.: On the decrease in transformation stress in a bicrystal Cu-Al-Mn shape-memory alloy during cyclic compressive deformation. Materials **14**(16) (2021)

[41] Bauer, A., Vollmer, M., Niendorf, T.: Effect of crystallographic orientation and grain boundaries on martensitic transformation and superelastic response of oligocrystalline Fe–Mn–Al–Ni shape memory alloys. Shape Memory and Superelasticity **7**(3), 373–382 (2021)

[42] Bouyra, Q., Blaysat, B., Chanal, H., Grédiac, M.: Using laser marking to engrave optimal patterns for in-plane displacement and strain measurement. Strain **58**(2), 12404 (2022)

[43] Oscarsson, J., Olsson, A., Enquist, B.: Strain fields around knots in Norway spruce specimens exposed to tensile forces. Wood Science and Technology **46**(4), 593–610 (2012)

[44] van Blokland, J., Olsson, A., Oscarsson, J., Daniel, G., Adamopoulos, S.: Crack formation, strain distribution and fracture surfaces around knots in thermally modified timber loaded in static bending. Wood Science and Technology **54**(4), 1001–1028 (2020)

[45] Chun-Wei, C., Far-Ching, L.: Strain concentration effects of wood knots under longitudinal tension obtained through digital image correlation. Biosystems Engineering **212**, 290–301 (2021)

[46] Grédiac, M., Sur, F.: Effect of sensor noise on the resolution and spatial resolution of the displacement and strain maps obtained with the grid method. Strain **50**(1), 1–27 (2014)

[47] Chrysochoos, A., Surrel, Y.: Chapter 1. Basics of metrology and introduction to techniques. In: Grédiac, M., Hild, F. (eds.) Full-field Measurements and Identification in Solid Mechanics, pp. 1–29 (2012). Wiley

[48] Wittevrongel, L., Lava, P., Lomov, S.V., Debruyne, D.: A self adaptive global digital image correlation algorithm. Experimental Mechanics **55**(2), 361–378 (2015)

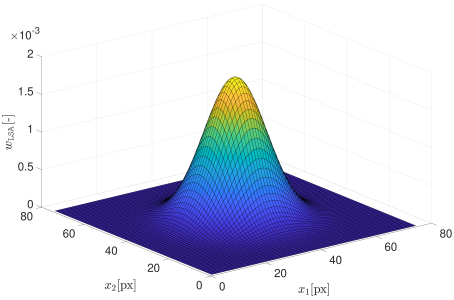

(a) Gaussian analysis window. Particular case with $\ell_{\mathsf{LSA}} = p = 9.3$ [px]

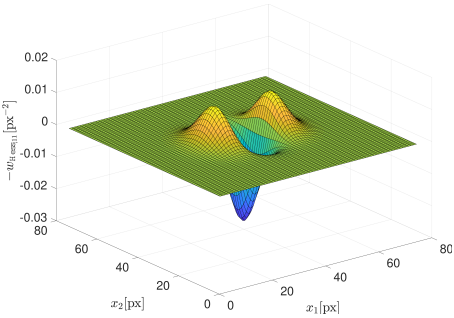

(b) Opposite of the second derivative kernel along x_1 (denoted by $w_{,11}$) with $\frac{\ell_{\mathsf{Hess}}}{\ell_{\mathsf{LSA}}} = 0.67$ [-] and $\ell_{\mathsf{LSA}} = p = 9.3$ [px]

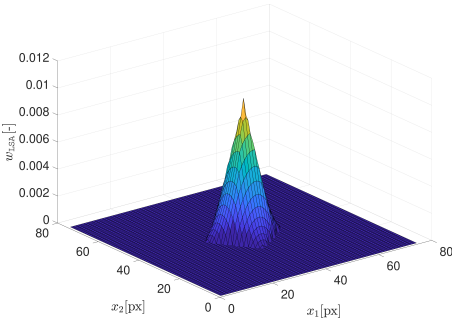

(c) Bi-triangular analysis window discussed in Section 5. The borders are aligned with the bisectors of the squares forming the checkerboard. Width $= 2\ell_{\mathsf{LSA}} = 2p = 18.6$ [px]

Fig. 2: (a)- and (c) Analysis windows. (b) Second derivative kernel.

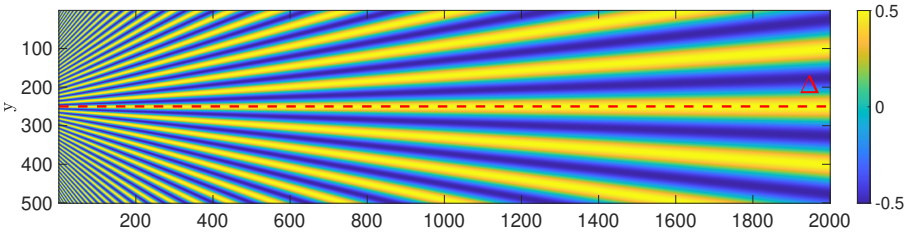

Fig. 3: Reference displacement field. Throughout the paper, the cross-section of the different u_2 displacement fields will be given along the midline Δ.

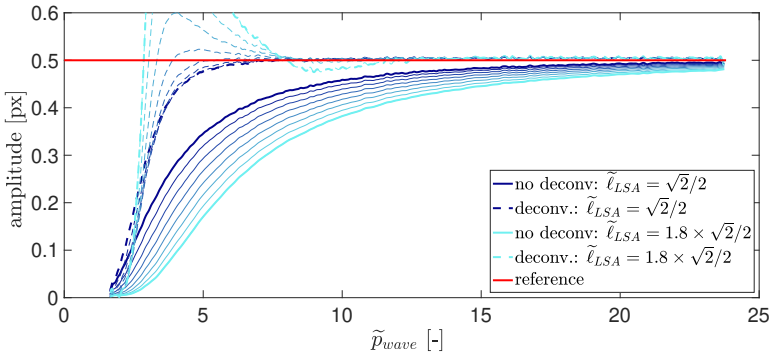

(a) Case 1: $\widetilde{\ell}_{\mathsf{Hess}}$ constant ($\widetilde{\ell}_{\mathsf{Hess}} = 0.70$ [-]) whatever the value of $\widetilde{\ell}_{\mathsf{LSA}}$

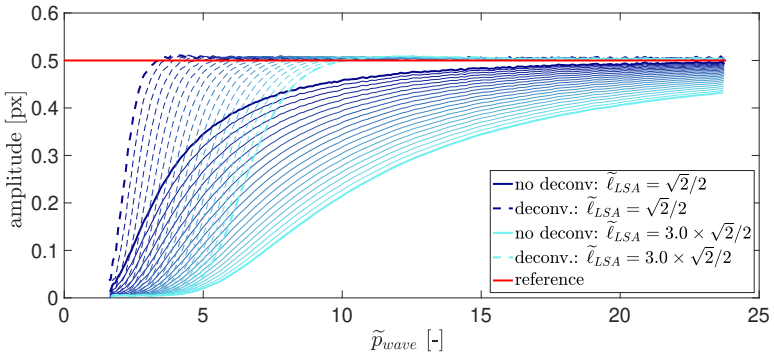

(b) Case 2: $\widetilde{\ell}_{\mathsf{Hess}}$ proportional to $\widetilde{\ell}_{\mathsf{LSA}}$, with $\widetilde{\ell}_{\mathsf{Hess}} = 0.70 \times \widetilde{\ell}_{\mathsf{LSA}}[-]$, noiseless data

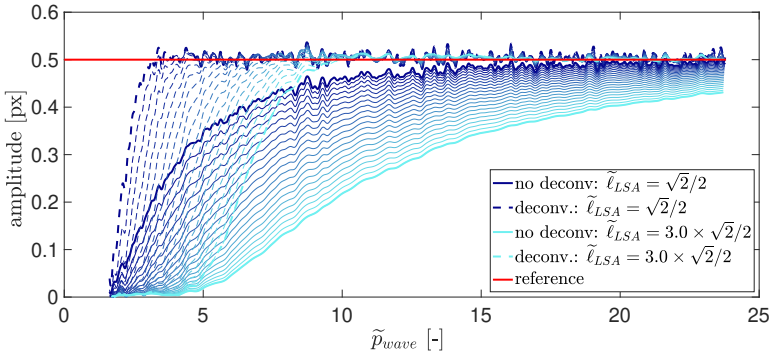

(c) Case 3: same as Case 2 above, but with noisy data

Fig. 4: Influence of $\widetilde{\ell}_{\mathsf{Hess}}$ on the convergence of the deconvolution algorithm, with $\widetilde{\ell}_{\mathsf{LSA}}$ increasing stepwise from $\sqrt{2}/2$ [-] to $2\sqrt{2}/2$ [-] (value of the step: $0.1 \times \sqrt{2}/2$ [-]). $\widetilde{\ell}_{\mathsf{Hess}}$ is constant in -(a), and proportional to $\widetilde{\ell}_{\mathsf{LSA}}$ in -(b) and -(c), with $\widetilde{\ell}_{\mathsf{LSA}} = 0.70 \times \widetilde{\ell}_{\mathsf{Hes}}$. The red line is the reference value of the amplitude along Δ: 0.5 [px].

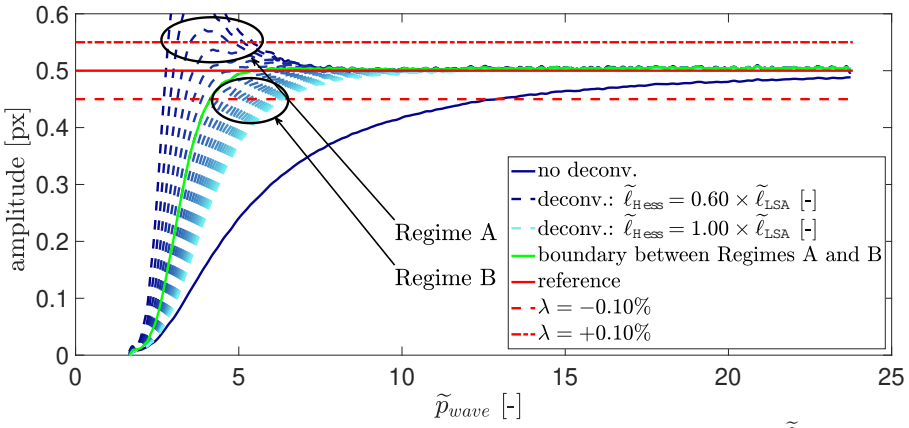

(a) Cross-section of the u_2 map along Δ for various values of the $\frac{\widetilde{\ell}_{\mathsf{Hess}}}{\widetilde{\ell}_{\mathsf{LSA}}}$ ratio

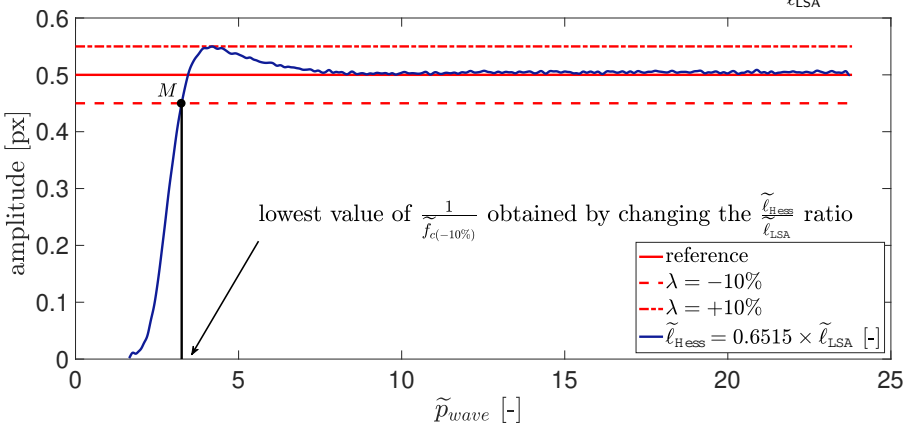

(b) Finding the lowest possible value of $\frac{1}{\widetilde{f}_{c(-10\%)}}$ for a given value of $\widetilde{\ell}_{\mathsf{LSA}}$

Fig. 5: Influence of $\widetilde{\ell}_{\mathsf{Hess}}$ on the convergence of the deconvolution algorithm, with $\widetilde{\ell}_{\mathsf{LSA}} = \frac{\sqrt{2}}{2} \times 1.4$ [-]. (a)- $\widetilde{\ell}_{\mathsf{Hess}}$ stepwise increases from 0.60 [-](dark blue) to 1.00 [-] (light blue), with a step equal to 0.02 [-]. The green curve is at the boundary between Regime A and B, characterized by $\widetilde{\ell}_{\mathsf{Hess}} = 0.72 \times \widetilde{\ell}_{\mathsf{LSA}}$ (b)- Determination of the lowest possible value of $\frac{1}{\widetilde{f}_{c(-10\%)}}$.

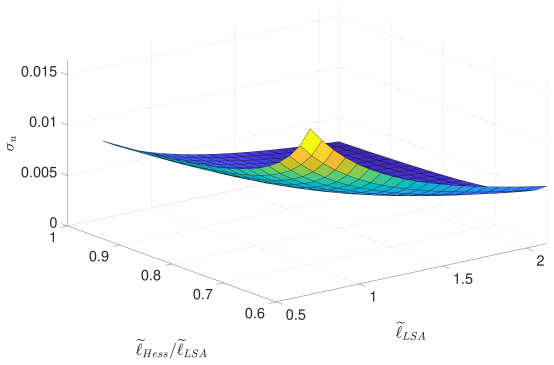

(a) Displacement resolution σ_u

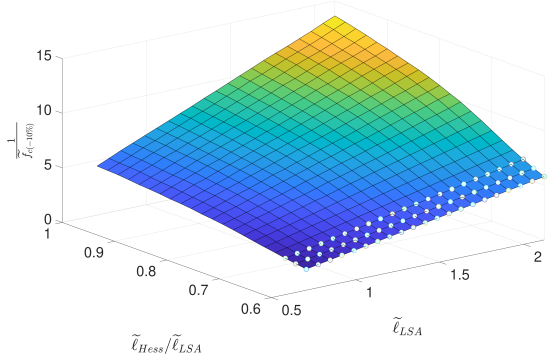

(b) Normalized spatial resolution $\frac{1}{\widetilde{f}_{c(-10\%)}}$

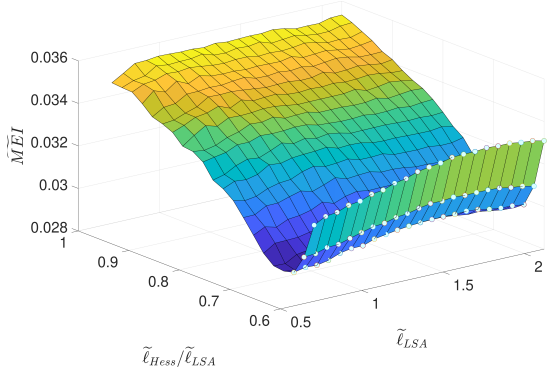

(c) $\widetilde{\text{MEI}} = \frac{\sigma_u}{\widetilde{f}_{c(-10\%)}}$

Fig. 6: Displacement resolution σ_u (a), normalized spatial resolution $\frac{1}{\widetilde{f}_{c(-10\%)}}$ (b) and normalized MEI ($\widetilde{\text{MEI}}$) (c) obtained after deconvolution as a function of the normalized standard deviation of the Gaussian window used in LSA $\widetilde{\ell}_{\mathsf{LSA}}$, and the $\frac{\widetilde{\ell}_{\mathsf{Hess}}}{\widetilde{\ell}_{\mathsf{LSA}}}$ ratio. In subfigures b- and c-, the points corresponding to the cases for which $\lambda > 10\%$ are highlighted. Simulations performed with ρ equal to 6.3 [px/period].

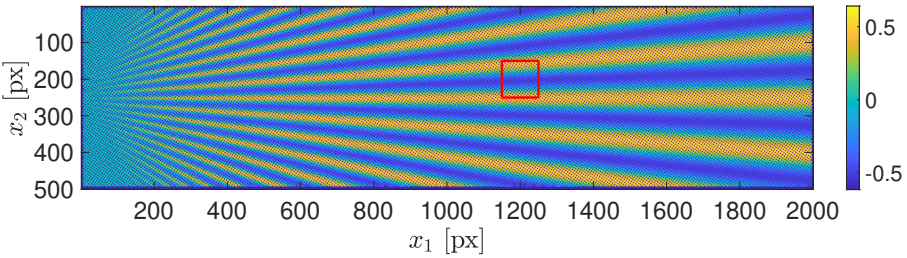

(a) u_2 displacement field and red square where closeup views are given in subfigures c- and d-

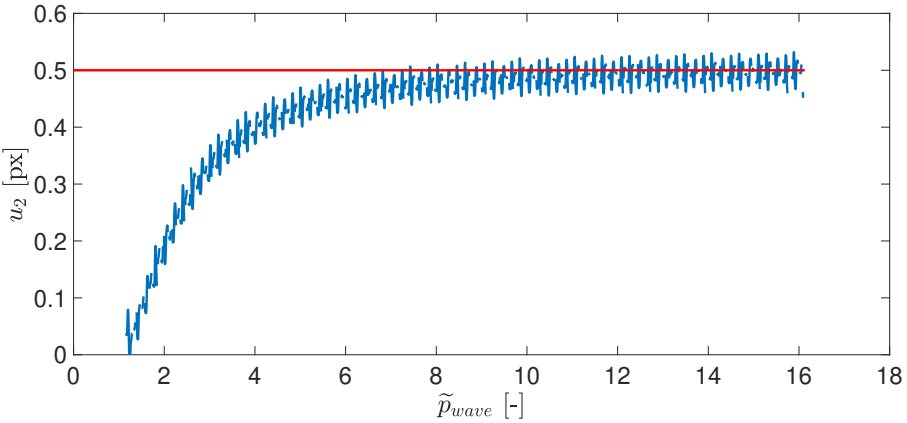

(b) Cross-section of the u_2 displacement field along Δ

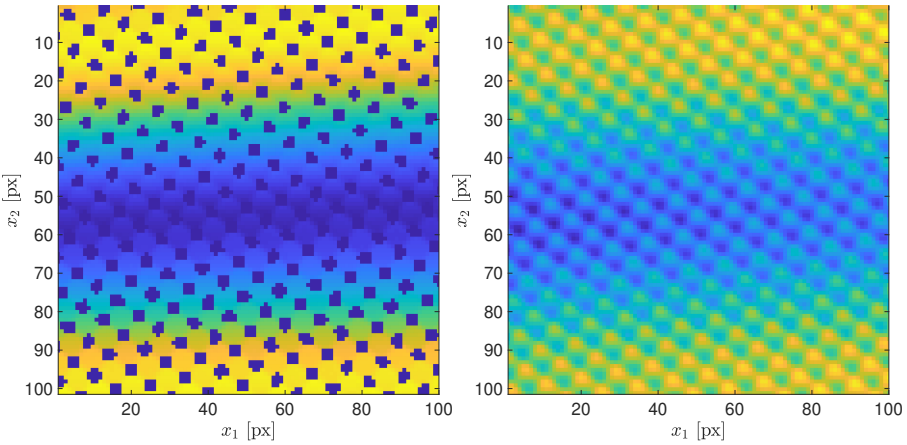

(c) Closeup view of the u_2 displacement field over the red square

(d) Closeup view of the phase distribution over the red square

Fig. 7: Results obtained after deconvolution, and by using LSA with a bitriangular analysis window of width equal to 2 times the nominal period of the checkerboard, with $\rho = 9.3$ [px].

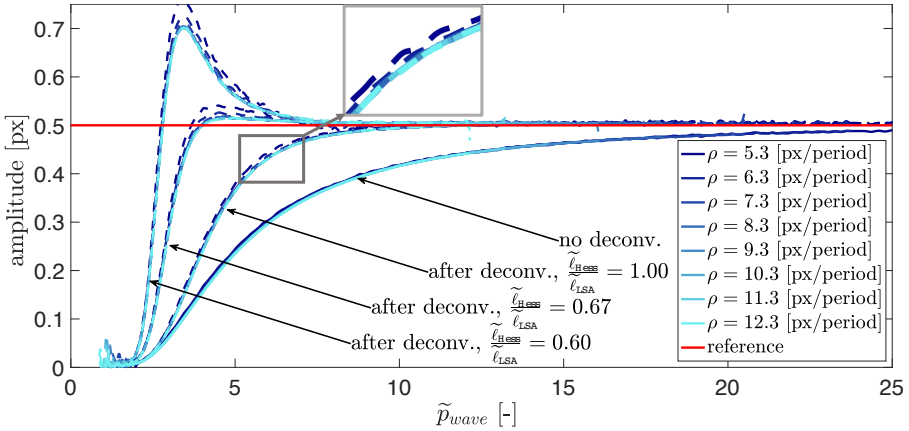

Fig. 8: For eight values of ρ, cross-section along Δ of the displacement field as a function of the normalized value $\widetilde{p}_{wave}$ of the sine wave of the reference displacement field. Normalization is performed with respect to ρ in each of the eight cases. The brighter the blue, the higher the value of ρ and thus the shorter the curves because of normalization. The closeup view shows that the dashed curves representing the results after deconvolution with $\frac{\widetilde{\ell}_{\text{Hess}}}{\widetilde{\ell}_{\text{LSA}}} = 1.00$ [-] are superposed, apart from the case $\rho = 5.3$ [-] for which it is slightly shifted.

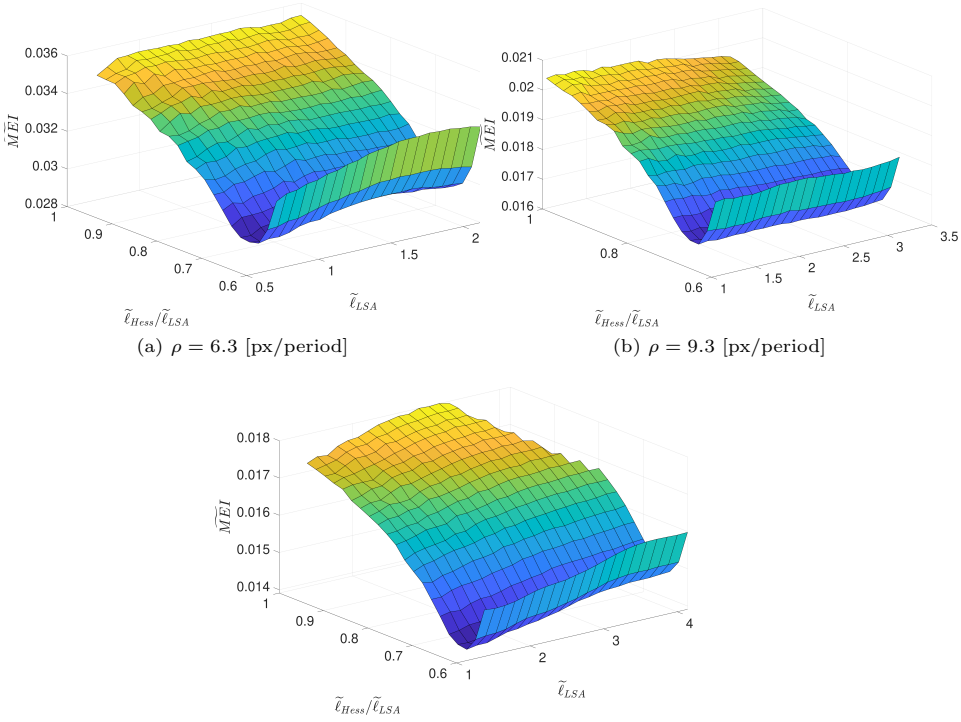

(a) $\rho = 6.3$ [px/period] (b) $\rho = 9.3$ [px/period]

(c) $\rho = 12.3$ [px/period]

Fig. 9: $\widetilde{\text{MEI}}$ as a function of $\widetilde{\ell}_{\mathsf{LSA}}$ and $\frac{\widetilde{\ell}_{\mathsf{Hess}}}{\widetilde{\ell}_{\mathsf{LSA}}}$ for three different values of the sampling density ρ.

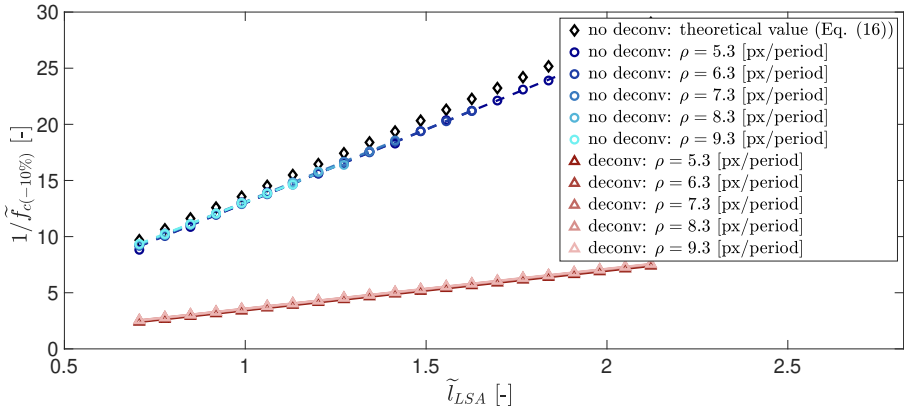

Fig. 10: Comparison between the values of the spatial resolution before and after deconvolution with the optimized value for the $\frac{\widetilde{\ell}_{\mathsf{Hess}}}{\widetilde{\ell}_{\mathsf{LSA}}}$ ratio and for $\widetilde{\ell}_{\mathsf{LSA}}$ lying between $\frac{\sqrt{2}}{2}$ and $3.0 \times \frac{\sqrt{2}}{2}$. Diamonds: results obtained with Equation 20. Other points: results from simulation obtained with noiseless synthetic images sampled $\rho \in \{5.3, 6.3, 7.3, 8.3, 9.3\}$ [-]. Dashed/solid lines: line fitting of the results obtained with simulated values of $\frac{1}{\widetilde{f}_c(-10\%)}$ before/after deconvolution.

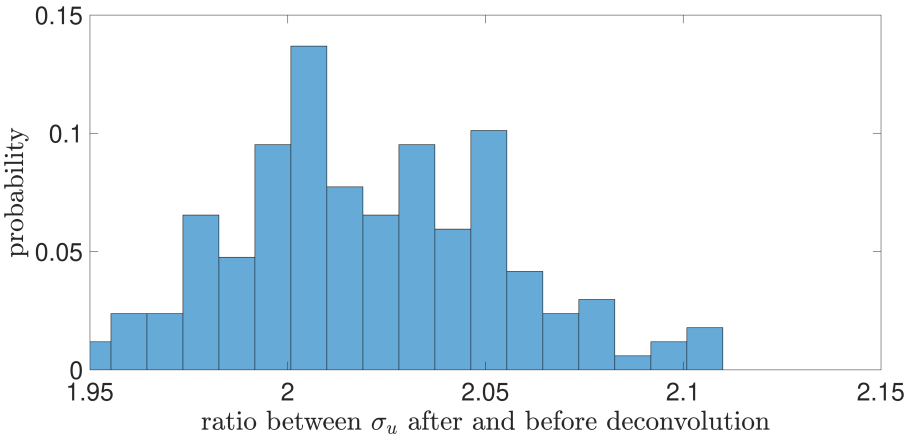

Fig. 11: Ratio between σ_u after and before deconvolution for the optimal value of the $\frac{\widetilde{\ell}_{\mathsf{Hess}}}{\widetilde{\ell}_{\mathsf{LSA}}}$ ratio (equal to 0.67), with $\rho \in \{5.3, 6.3, 7.3, 8.3, 9.3, 10.3, 11.3, 12.3\}$ [px/period], and $\widetilde{\ell}_{\mathsf{LSA}} \in \{1.0 \times \frac{\sqrt{2}}{2}, 1.1 \times \frac{\sqrt{2}}{2}, \cdots, 2.9 \times \frac{\sqrt{2}}{2}, 3.0 \times \frac{\sqrt{2}}{2}\}$ [px/period]. Mean value of this ratio: 2.02 [-].

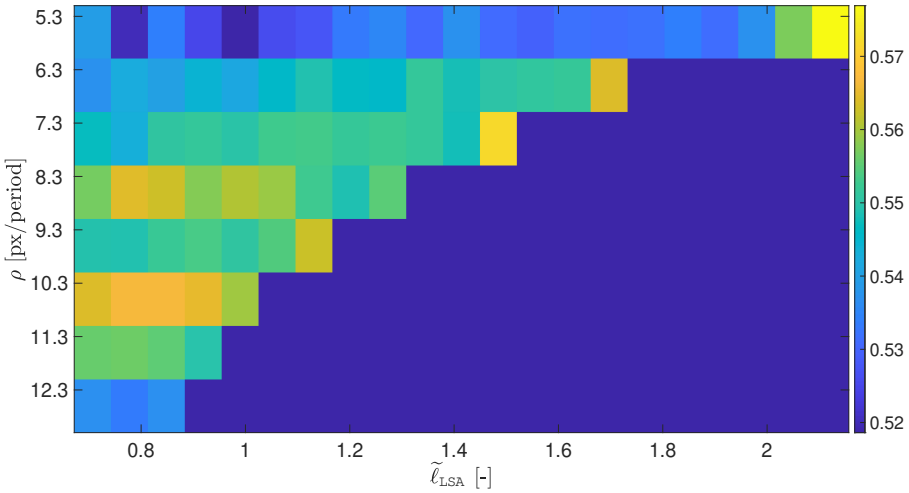

Fig. 12: Ratio between $\widetilde{\mathrm{MEI}}$ after and before deconvolution for the optimal value of the $\frac{\widetilde{\ell}_{\mathrm{Hess}}}{\widetilde{\ell}_{\mathrm{LSA}}}$ ratio (equal to 0.67), with $\rho \in \{5.3, 6.3, 7.3, 8.3, 9.3\}$ [px/period], and $\widetilde{\ell}_{\mathrm{LSA}} \in \{1.0 \times \frac{\sqrt{2}}{2}, 1.1 \times \frac{\sqrt{2}}{2}, \cdots, 2.9 \times \frac{\sqrt{2}}{2}, 3.0 \times \frac{\sqrt{2}}{2}\}$ [-]. Mean value of this ratio: 0.547 [-]. Defined only when $\frac{1}{\widetilde{f}_{c(-10\%)}}$ can be found by graphical construction from the reference displacement field retrieved before deconvolution.

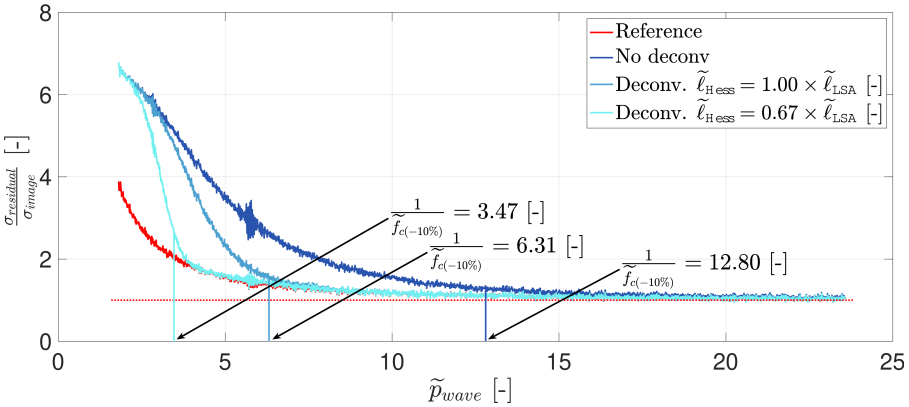

Fig. 13: Standard deviation of the normalized residual calculated column wise before and after deconvolution with (0.67) and without (1.00) optimal $\frac{\widetilde{\ell}_{\mathrm{Hess}}}{\widetilde{\ell}_{\mathrm{LSA}}}$ ratio. The normalized spatial resolution $\frac{1}{\widetilde{f}_{c(-10\%)}}$ is reported in each of the three cases.

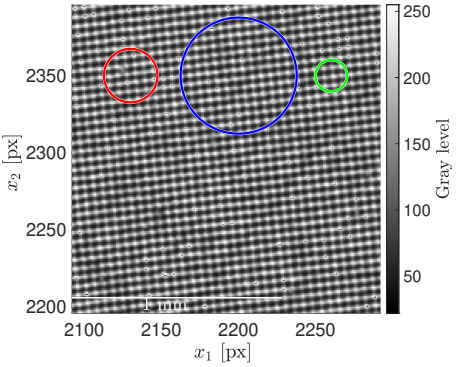

Fig. 14: Closeup view of the pattern printed by laser marking on the SMA specimen. Size of the black or white squares forming the checkerboard: 30 microns. Red circle: apparent size of the Gaussian window used in LSA according to the "3-σ rule" [16]. The diameter of the blue (resp. green) circle is equal to $\frac{1}{f_{c(-10\%)}}$ before (resp. after) deconvolution. Sampling density $\rho = 8.2$ [px/period]. The pattern is slightly inclined to avoid aliasing [17]. The effect on the phase maps of the printing defects which are visible in this picture are compensated by the fixed-point algorithm used when solving numerically Equation 2.

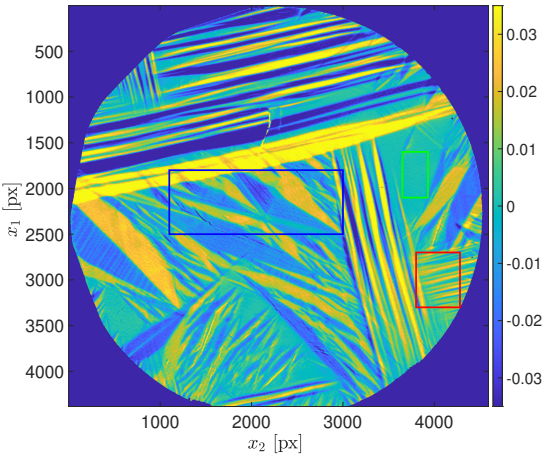

(a) U_{12} before deconvolution [-]

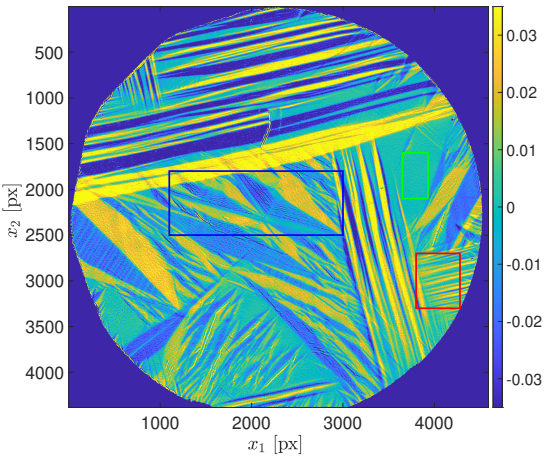

(b) U_{12} after deconvolution [-]

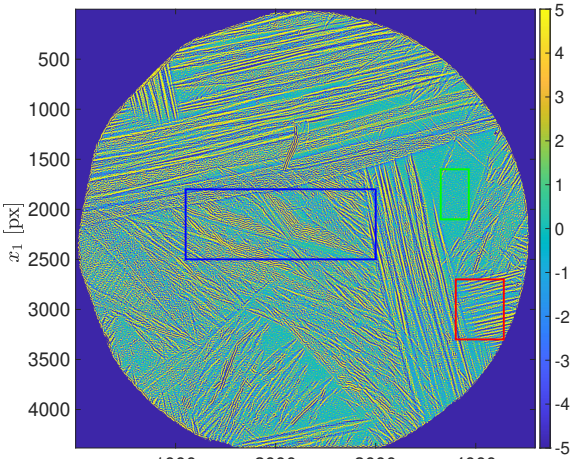

(c) Difference $\times 10^{-3}$ [-]

Fig. 15: Typical U_{12} maps before and after deconvolution. The diameter of the specimen is equal to 3.5 cm. The reader is invited to zoom in the electronic version of the paper in order to appreciate the details.

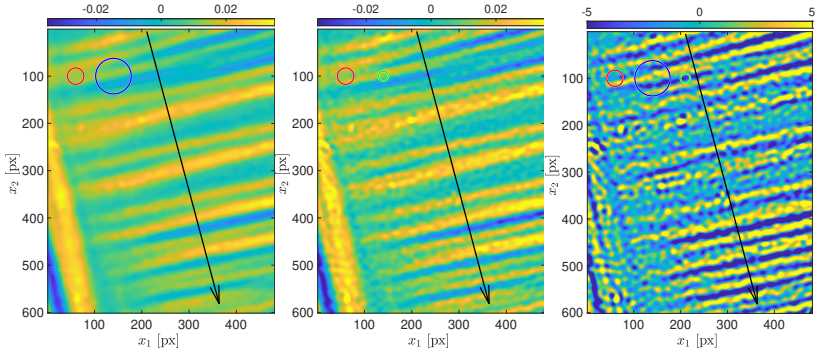

(a) U_{12} [-] before deconvolution (b) U_{12} [-] after deconvolution (c) Difference $\times 1E-03$ [-]

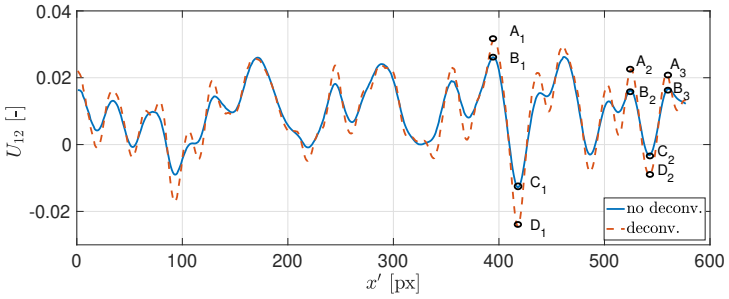

(d) U_{12} [-] along the black line

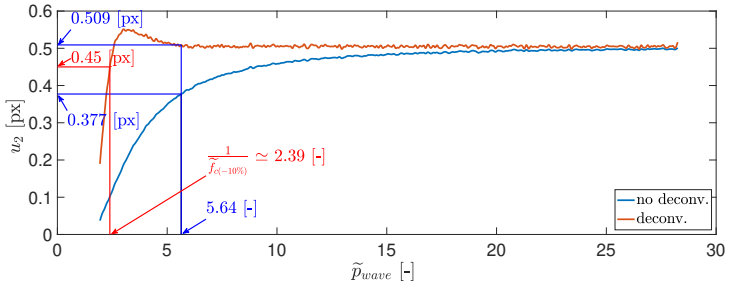

(e) Curve along Δ for $\widetilde{\ell}_{\mathsf{LSA}} = \frac{\sqrt{2}}{2}$ [-] and $\frac{\widetilde{\ell}_{\mathsf{Hess}}}{\ell_{\mathsf{LSA}}} = 0.67$ [-]

Fig. 16: Closeup view of the red rectangle in the U_{12} maps before and after deconvolution. Size: 3.54×4.42 mm^2.

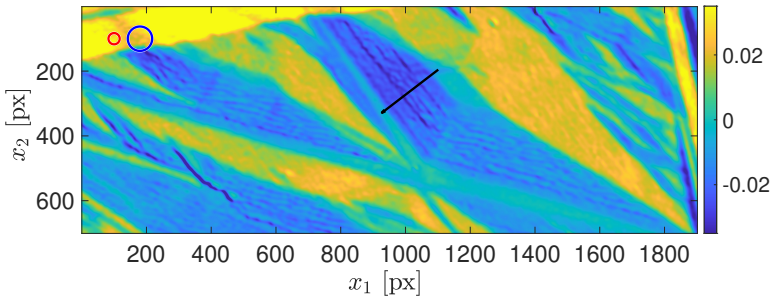

(a) U_{12} [-] before deconvolution

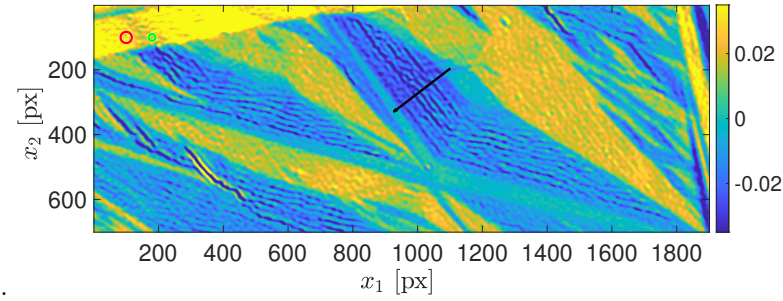

(b) U_{12} [-] after deconvolution

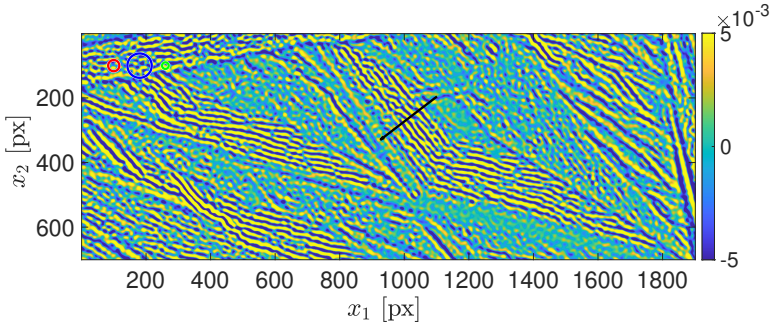

(c) Difference [-]

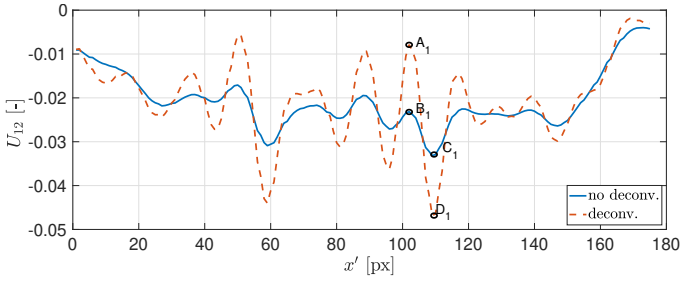

(d) U_{12} [-] along the black line

Fig. 17: Closeup view of the blue rectangle in the U_{12} maps before and after deconvolution. Size: 13.98×5.15 mm^2.

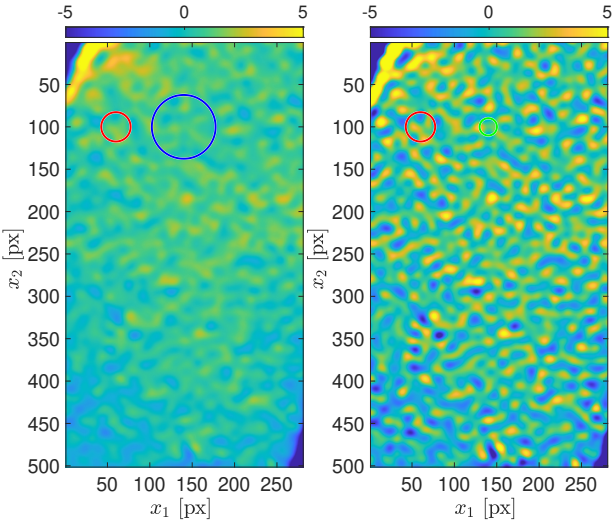

(a) U_{12} [-] before deconvolution ($\times 1E-03$)

(b) U_{12} [-] after deconvolution ($\times 1E-03$)

Fig. 18: Closeup view of the green rectangle in the U_{12} maps before and after deconvolution. Size: 2.07×3.68 mm^2.

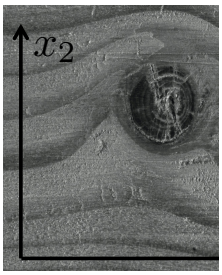

(a) Zone of interest (approximate location), after [42]

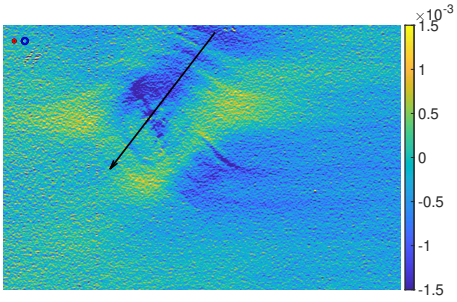

(b) Case 1: $\widetilde{\ell}_{\mathsf{LSA}} = 1 \times \frac{\sqrt{2}}{2}$, no deconv.

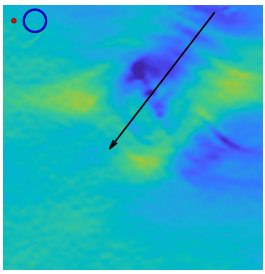

(c) Case 2a: $\widetilde{\ell}_{\mathsf{LSA}} = 3.68 \times \frac{\nu_c}{2}$, no deconv.

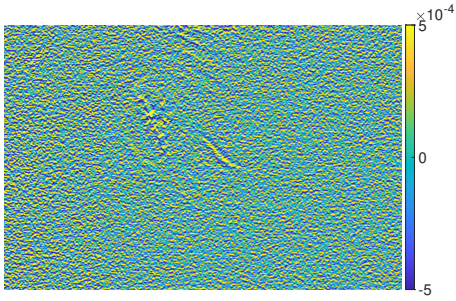

(d) difference between (c) and (b)

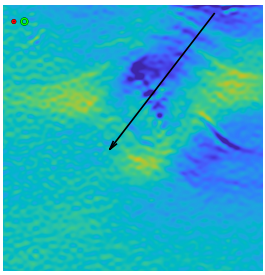

(e) Case 2b: $\widetilde{\ell}_{\mathsf{LSA}} = 3.68 \times \frac{\nu_c}{2}$, deconv.

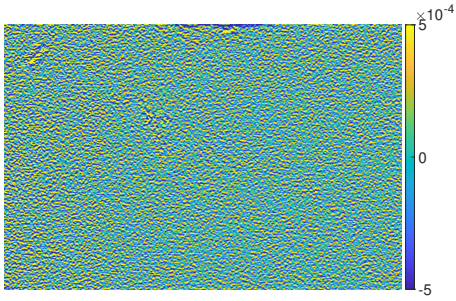

(f) Difference between (e) and (b)

Fig. 19: Zone of interest and ε_{22} strain maps obtained with various settings. Red, blue and green circles: same definition as in the preceding example, see Section 8.1. The diameter of the green circle in subfigure (e) is the same as the diameter of the blue circle in subfigure (b).

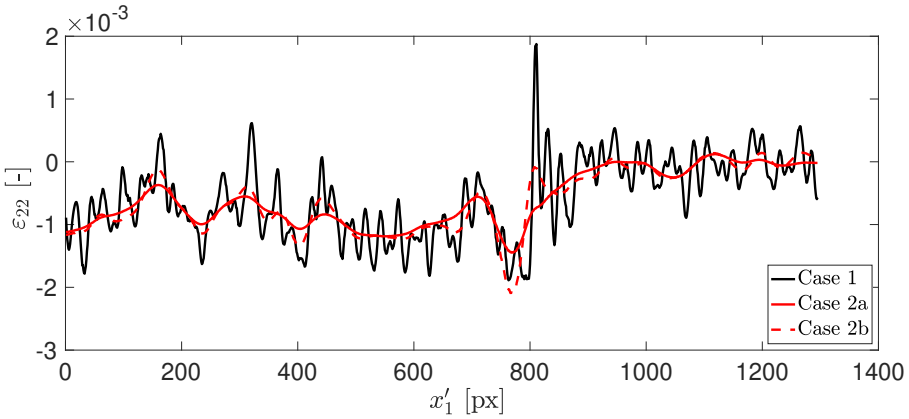

Fig. 20: Cross-section of the ε_{22} strain map obtained with different settings along the portion of line shown in Figures 19 (b),(c) and (e).

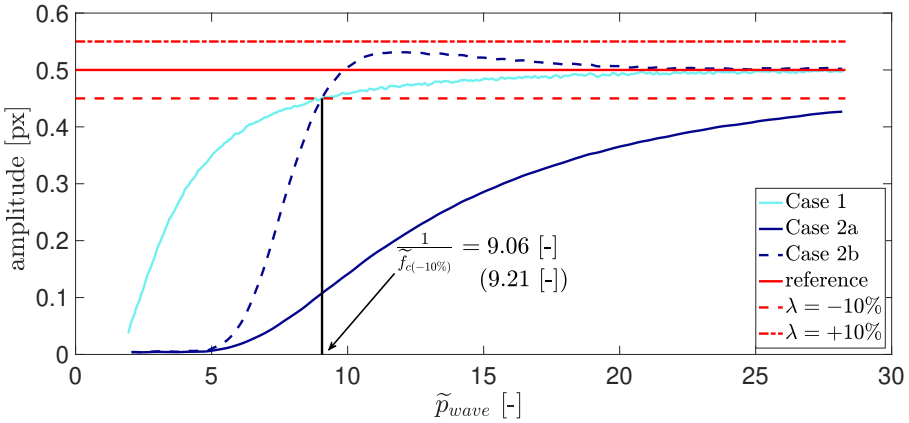

Fig. 21: Cross-section along Δ of the displacement field retrieved with the same settings of Cases 1, 2a, and 2b, but from synthetic images deformed with the reference displacement field shown in Figure 3.